SAE INTERNATIONAL

ARTICLE INFO
Article ID: 03-19-01-0003

doi:10.4271/03-19-01-0003

The Membrane Engine: Concept, Model, and First Results

***Roland Allmägi*[1] *and Risto Ilves*[1]**

[1]*Estonian University of Life Sciences, Institute of Forestry and Engineering, Chair of Biosystems Engineering, Estonia*

Abstract

This study investigates the feasibility of a novel internal combustion engine (ICE) architecture, termed the membrane engine, in which the conventional piston is replaced by a flexible elastic membrane. Although the concept appears in several patent documents proposing reduced friction, improved sealing, and lower heat losses, no empirical data has been published to support these claims. To the authors' knowledge, this work presents the first membrane engine built and experimentally tested. The primary aim is to verify whether such an engine can operate as a functional ICE, regardless of its current efficiency or performance level.

To support concept validation, a simplified mathematical model was developed to describe the membrane's deformation and its effect on combustion chamber volume. Unlike conventional piston engines, the membrane introduces a pressure-dependent geometry, enabling a variable compression ratio. The model is not intended to predict performance but to assist in interpreting experimental results and assessing feasibility. It combines geometric and pressure-induced volume changes and was constructed conservatively to avoid overestimating deformation effects.

A single-cylinder spark-ignition prototype was built by modifying an existing piston engine. Experimental tests were conducted under motored and fired conditions, with comparative measurements taken against the unmodified engine. Results confirmed that the membrane engine can sustain combustion and produce torque. Notably, the exhaust stroke exhibited a steeper pressure drop, suggesting improved scavenging, and the torque trace showed a distinct positive spike post-combustion. These findings support the hypothesis that the membrane's dynamic behavior influences combustion and gas exchange.

While some patent claims remain unverified, the study demonstrates that the membrane engine is a viable concept. The results provide a foundation for further development and refinement, including material selection and advanced modeling. Future work will focus on improving durability, expanding the operating envelope, and exploring hybrid configurations for waste heat recovery.

History

Received: 23 Jul 2025
Revised: 18 Dec 2025
Accepted: 22 Jan 2026
e-Available: 12 Feb 2026

Keywords

Membrane engine, Variable compression ratio, Alternative piston design, Pressure-dependent volume, Experimental validation, Internal combustion engine modeling, Dynamic combustion chamber geometry, Elastic energy recovery, Instantaneous torque analysis, Elastomer strain modeling

Citation

Allmägi, R. and Ilves, R., "The Membrane Engine: Concept, Model, and First Results," *SAE Int. J. Engines* 19(1):43-68, 2026, doi:10.4271/03-19-01-0003.

ISSN: 1946-3936
e-ISSN: 1946-3944

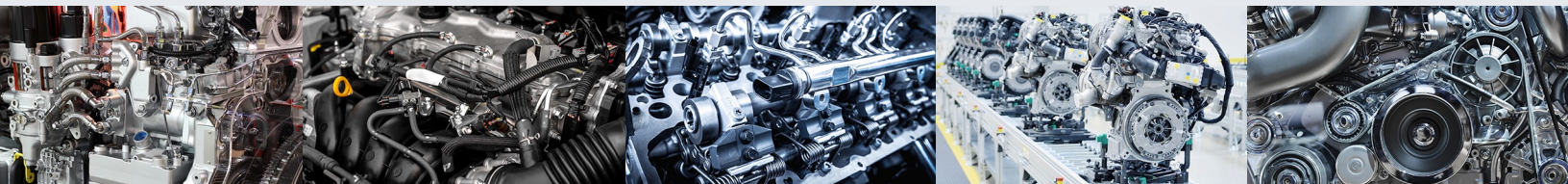

1. Introduction

The reciprocating piston engine (PE) remains a dominant power source in transportation and stationary applications [1, 2]. Despite decades of refinement, the growing demand for cleaner and more efficient engines continues to drive innovation [3–5].

Current research efforts focus on improving thermal efficiency to reduce fuel consumption and emissions [5–7]. Although modern PEs achieve up to 40% efficiency, significant energy is still lost as heat [7, 9]. To increase the usable fraction of fuel energy and mitigate the environmental impact of internal combustion engines (ICEs), new approaches are being explored. These include reducing heat losses, optimizing combustion chamber insulation, and developing advanced fuel injection strategies [5, 10–13].

In parallel, alternative engine architectures are being investigated to overcome the inherent limitations of the conventional four-stroke PE. These concepts often involve variable compression ratios and stroke lengths, achieved through dynamic changes in engine geometry [14–27].

The piston itself is a critical component, subject to high thermal and mechanical loads. Together with the rings and cylinder wall, it forms a major friction pair, contributing significantly to mechanical losses [28–34]. This sliding assembly requires continuous lubrication, and its failure can occur within minutes if lubrication is interrupted. Due to this design, complete sealing between the combustion chamber and crankcase is not possible, resulting in blow-by of combustion gases and migration of lubricating oil into the combustion chamber, both of which contribute to emissions [35–38].

Replacing the conventional piston with a flexible membrane capable of transmitting combustion energy to the crankshaft offers a novel alternative [39–43]. The membrane engine shares key operational principles with piston engines and piston compressors, where reciprocating motion is used to compress and displace gases. This analogy extends to diaphragm compressors, which similarly employ a flexible membrane to achieve gas displacement [44, 45]. These analogies allow established ICE modeling frameworks to be adapted for membrane-based systems, enabling theoretical analysis and performance prediction.

Although numerous patent documents describe membrane-based engine concepts, none report a functioning prototype or any experimental validation [39–43]. The novelty of the present work lies in providing, to the authors' knowledge, the first physical prototype of an ICE operating with an elastic membrane, together with its experimental testing under both motored and fired conditions. This establishes a practical foundation for evaluating the membrane engine concept beyond the theoretical claims made in earlier patents.

To identify a feasible design, the authors conducted a comprehensive patent review using databases such as EPO, WIPO, DPMA, USPTO, and Google Patents. Keywords included membrane engine, membrane motor, and disk engine, with care taken to exclude unrelated results from carburetor or vacuum systems. IPC classification F02B75/36 (engines with resilient chamber walls) was used, while F04B43/02 (flexible diaphragm pumps) was excluded due to its focus on non-power–generating machines.

Through critical analysis, approximately 10 patents were selected for further review. While many documents proposed efficiency improvements and solutions to PE drawbacks, only a few were deemed suitable for prototype development [39–43]. Selection criteria included simplicity of membrane design, elastic behavior, and mechanical linkage to the crankshaft. Designs relying on bellows or hydraulic power transfer were excluded.

This study presents a preliminary investigation into the membrane engine concept, aiming to validate its feasibility through prototype construction and modeling. The focus is on demonstrating that the concept can function as an ICE, rather than proving performance superiority.

One commonly proposed advantage in patent literature is the potential reduction in the number of sliding and reciprocating components within the engine. This simplification could reduce frictional losses and allow a greater proportion of generated energy to be converted into useful work [39–43].

Studies indicate that mechanical losses account for up to 30% of total energy losses in piston engines, with approximately 70% of those occurring in the piston assembly [28, 41]. Various strategies have been explored to reduce piston friction, and one such approach is the membrane engine, which may offer several advantages in minimizing internal resistance.

Additionally, the membrane could provide a complete seal between the combustion chamber and crankcase, potentially eliminating blow-by and its associated losses, wear, and emissions, as suggested in several patents [40, 42].

A significant portion of heat losses in piston engines occurs through the exposed cylinder walls, especially as the piston moves toward bottom dead center (BDC). In contrast, the membrane engine confines combustion gases to contact only the elastic membrane, which may act as a thermal barrier. This configuration could theoretically reduce heat transfer to the cylinder walls and improve thermal efficiency, as supported by studies on thermal barrier coatings [12, 13, 46, 47].

The membrane engine is a reciprocating engine that has several similarities to a PE (Figure 1). In the design presented in this study, an elastic membrane seals the combustion chamber from the crankcase. Combustion gases flex the membrane downward, increasing the cylinder volume at BDC. At top dead center (TDC), the membrane returns to its original position, minimizing the volume. Unlike pistons, membranes deform rather than translate, enabling variable stroke and compression.

FIGURE 1 Working principle of the membrane engine (right) compared to a piston engine (left).

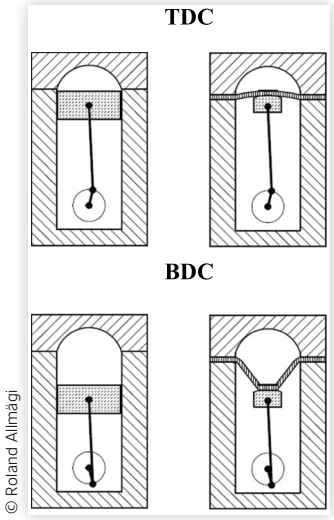

The aim of this study is to validate the concept of a novel membrane engine by constructing a prototype and modeling its combustion chamber volume. Unlike rigid pistons, the membrane deforms under pressure, resulting in a dynamically changing chamber geometry. Due to structural and operational similarities with conventional piston engines, established ICE theory can be partially adapted to describe its behavior, particularly in terms of crankshaft kinematics and cycle timing. However, conventional theory does not account for elastic combustion chamber boundaries, which necessitates a fundamentally different modeling approach. The pressure-dependent volume model presented in this study is therefore a simplified empirical construct, developed to assess whether membrane deformation under combustion pressure can produce measurable effects. It is not intended as a predictive or physically complete model. Rather, it serves as a conceptual tool to support the feasibility of the membrane engine architecture.

2. Materials and Methods: Concept, Modeling, and Experimental Setup

2.1. Reciprocating PE Model

In a reciprocating PE, combustion gases exert force on the piston, driving it downward and rotating the crankshaft. This motion alters the cylinder volume cyclically minimum at TDC and a maximum at BDC. The clearance volume V_c is the volume at TDC, while the displacement volume V_d is swept by the piston between TDC and BDC. Their sum defines the total cylinder volume, and their ratio determines the compression ratio (CR) [9].

Cylinder volume depends on piston position, which can be mathematically described by the distance $s(\theta)$ between the crankshaft and piston pin axes. The instantaneous cylinder volume $V(\theta)$ is calculated with Equation 1 as follows [9]:

$$V(\theta) = V_c + \left(a + l - \left[\sqrt{l^2 - a^2 \cdot \sin^2 \theta} + a \cdot \cos \theta \right] \right) \cdot \frac{\pi \cdot B^2}{4} \quad (1)$$

where

$V(\theta)$ is the instantaneous volume of the cylinder m^3;
V_c is the clearance volume m^3;
a is the crank radius m;
θ is the crankshaft position °;
l is the connecting rod length m;
B is the cylinder bore m.

where V_c remains constant, while the second term represents the dynamic volume based on piston stroke and bore area. This formulation enables precise modeling of cylinder volume throughout the engine cycle.

2.2. Simplified Cylinder Volume Model of the Membrane Engine

As a flexible component, the membrane changes shape throughout the engine cycle. This requires more complex mathematical descriptions to accurately model the instantaneous cylinder volume.

In a simplified model (Figure 2), the membrane is assumed to move vertically, with its central clamping disk (2) defining the displacement. Similar to PEs, the membrane's position relative to the crankshaft axis determines the combustion chamber volume. The membrane can be designed to lie relatively flat when the crankshaft is at 90° ATDC, which corresponds to the midpoint between TDC and BDC. Movement in either direction alters the volume above the membrane.

Assuming a flat central disk (2) remains rigid during deformation, the membrane can be approximated as forming a truncated cone. In Figure 2, the lower diameter D corresponds to the cylinder bore, and the upper diameter d to the clamping disk. For simplicity, the membrane is modeled as a uniform truncated cone whose height h varies with crankshaft angle. In this model, it is assumed that the membrane shape is governed solely by crankshaft position, and no additional forces act on the membrane surface. As a result, the membrane maintains a uniform conical shape throughout the cycle. The volume occupied by the membrane is described using the standard formula for a truncated cone, using Equation 2.

FIGURE 2 Principle drawing of the membrane engine cylinder volume (1—elastic membrane; 2—rigid center clamping disk; *d*, *D*, *h*—upper and lower diameters and height of the truncated cone, respectively).

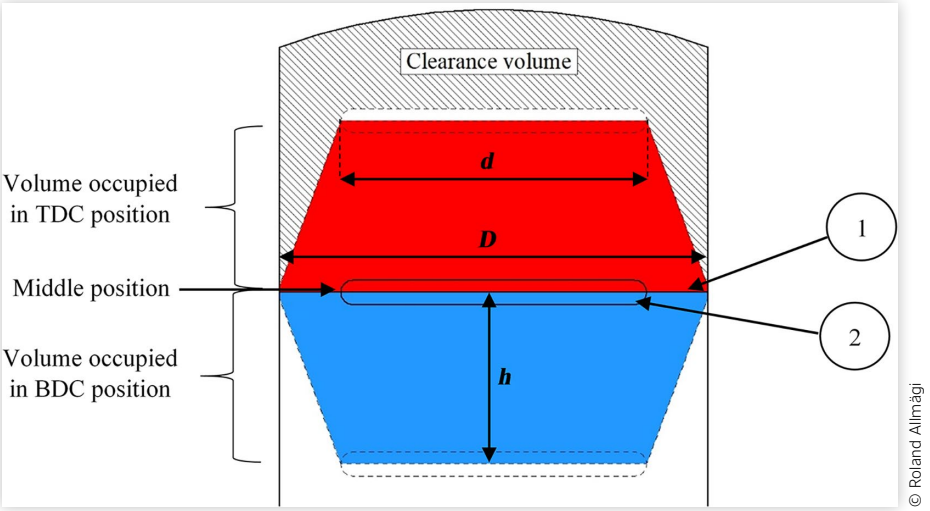

$$V_m = \frac{\pi \cdot h}{12} \cdot \left(D^2 + d^2 + D \cdot d\right) \quad (2)$$

where
V_m is the volume of the conical membrane m^3;
h is the cone height m;
D is the lower diameter of truncated cone m;
d is the upper diameter of truncated cone m.

Since the clearance volume remains constant, the change in cylinder volume during the cycle is attributed to membrane motion. The membrane forms two opposing truncated cones during its stroke, and the total displacement volume is expressed with Equation 3:

$$V_d = V_{c1} + V_{c2} \quad (3)$$

where
V_d is the engine displacement m^3;
V_{c1} is the upper truncated cone volume m^3;
V_{c2} is the lower truncated cone volume m^3.

Combining Equations 2 and 3 above with the PE volume model Equation 1 yields Equation 4 for the membrane engine's instantaneous volume as a function of crank angle:

$$V(\theta) = V_c + \frac{\pi \cdot h_1}{12} \cdot \left(d^2 + d \cdot B + B^2\right) - \frac{\pi \cdot \left(h_1 - a + \sqrt{l^2 - a^2 \cdot \sin\theta^2} + a \cdot \cos\theta - \sqrt{l^2}\right)}{12} \cdot \left(d^2 + d \cdot B + B^2\right) \quad (4)$$

where
$V(\theta)$ is the membrane engine instantaneous cylinder volume m^3;
V_c is the combustion chamber volume m^3;
h_1 is the height of the upper cone at TDC m;
B is the upper diameter of the membrane (cylinder bore) m;
d is the lower diameter of the membrane (membrane fastening disk) m;
a is the crank radius m;
l is the connecting rod length m;
θ is the crankshaft position °.

As described in Figure 2, the upper cone decreases the combustion chamber volume, and the lower cone increases the chamber volume. This must be considered when modeling the instantaneous volume of the membrane engine. The first term represents the volume when the membrane is flat, while the second term accounts for the dynamic volume change due to membrane deformation. This model captures the membrane's influence on combustion chamber geometry throughout the cycle.

2.2.1. Actual Engine Geometry Considerations While Setting Up the Model While the simplified membrane engine model illustrates the principle of volume change during the cycle, it does not fully capture the membrane's actual shape, which is influenced by mechanical constraints and pressure fluctuations. Membrane thickness also affects internal and external volumes depending on engine position.

Preliminary experiments on a test rig (Figure 3) confirm that under ambient pressure, the membrane forms a truncated cone, consistent with the simplified model.

FIGURE 3 Stretched membrane in BDC position in the test bench.

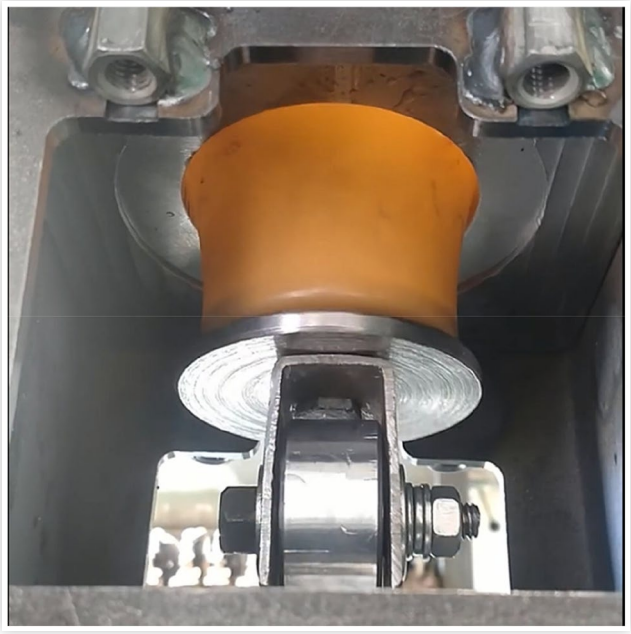

TABLE 1 Piston engine DB3500CL parameters.

Strokes	4	Connection rod length	84.8 mm
Cylinder	1	Crankshaft radius	27 mm
Engine power	3.6 kW	Bore	70.00 mm
Speed	3000 rpm	Stroke	54.00 mm
Fuel supply system	Carburetor	Displacement volume	207.42 cm^3
Ignition system	Magneto spark ignition	Clearance volume	28.28 cm^3
Compression ratio	8	Total volume	235.7 cm^3

However, unlike the idealized sharp-edged cone, real membranes exhibit curved transitions at fixation points and may form concave surfaces. These deformations depend on material properties and applied forces. Therefore, while the model focuses on displaced volume rather than exact geometry, adjustments must account for nonuniform membrane behavior between TDC and BDC.

The first prototype was built by modifying a single-cylinder, naturally aspirated petrol engine (Figure 4), while retaining similar mechanical constraints to the original PE, with its parameters provided in Table 1. The membrane is clamped between the cylinder head and block using large aluminum plates to ensure sealing with minimal force. To accommodate this, the pushrod assembly was relocated outside the cylinder head without altering valve timing or lift.

The modified engine will be tested under similar conditions to the unmodified engine to establish a baseline for test results.

The membrane shape, and thus the cylinder volume, varies throughout the four strokes of the Otto cycle. A cross-sectional schematic of the prototype membrane engine in TDC and BDC positions is shown in Figure 6. At TDC, the membrane is likely pressed firmly against the rigid guiding member (Figure 5) by combustion pressure, resulting in a relatively flat or slightly domed shape. During the intake stroke at BDC, the membrane is pulled downward and stretched into a conical form. The resulting pressure drop may cause the membrane walls to curve inward toward the central axis if the pressure differential exceeds the membrane's internal restoring forces.

Based on the created mathematical models in the previous section, the shape of the membrane at TDC (red) and BDC (blue) positions can be simplified to two truncated cones, as depicted in Figure 7. In this

FIGURE 4 Original piston engine (left) and the membrane engine prototype (right).

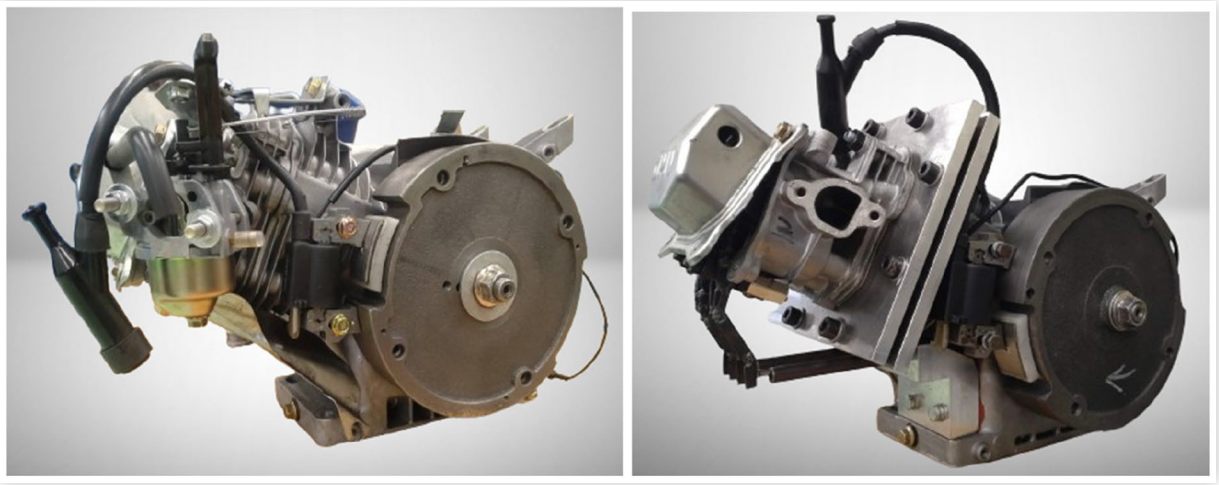

FIGURE 5 Guiding member for membrane fastening within the engine cylinder bore.

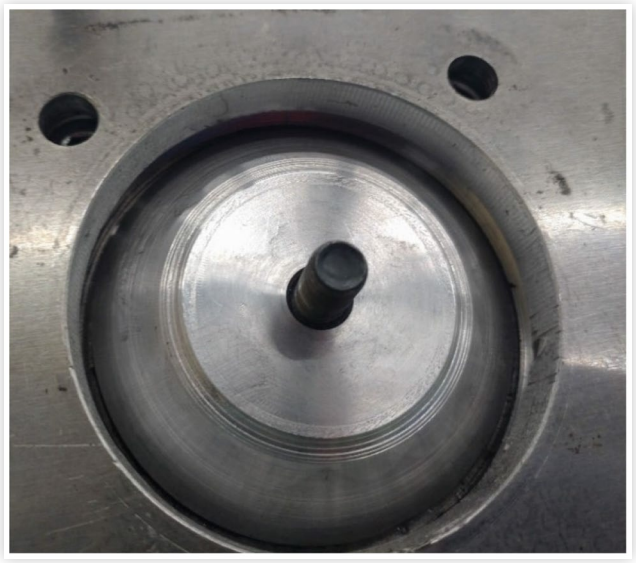

configuration, the lower cone has a larger volume than the upper cone. Therefore, the height h_1 portion of the membrane stroke in Equation 4 must be measured to correctly model the membrane engine cylinder volume.

The combustion chamber itself (shown in gray in Figures 6 and 7 in yellow) can be simplified as a dome, as its shape does not affect the volume it occupies. Thus, the entire membrane engine geometry can be modeled as a cylinder with a domed top (Figure 7 yellow) and a membrane forming two opposing truncated cones. Table 2 presents the measured and calculated parameters of the prototype membrane engine used for modeling.

This geometric model forms the basis for analyzing the membrane engine's dynamic volume changes and performance characteristics.

2.3. Pressure-Dependent Cylinder Volume Model

2.3.1 Modeling the Shape of the Membrane during Combustion During prototype development, it was hypothesized that high combustion pressure could deform the membrane against the cylinder wall, replacing the lower truncated cone with a domed cylinder shape (Figure 8).

While this could be approximated using the PE volume model (Equation 1), adjusted for membrane thickness, such simplification neglects the material-dependent threshold at which pressure overcomes membrane stiffness. Since this deformation may occur variably between BDC and TDC, assuming a fixed cylindrical shape during compression is inadequate. Therefore, a pressure-dependent term must be added to Equation 4 to account for this behavior, requiring a geometric and material-specific model of membrane deformation.

2.3.2. Stretching of the Membrane Although many materials are well-characterized, elastomers often require case-specific testing due to their complex behavior under load. The membrane's displacement and stress during

FIGURE 6 Cross-sectional schematic of the prototype engine cylinder volume at TDC (left) and BDC (right) with the combustion chamber volume in solid gray.

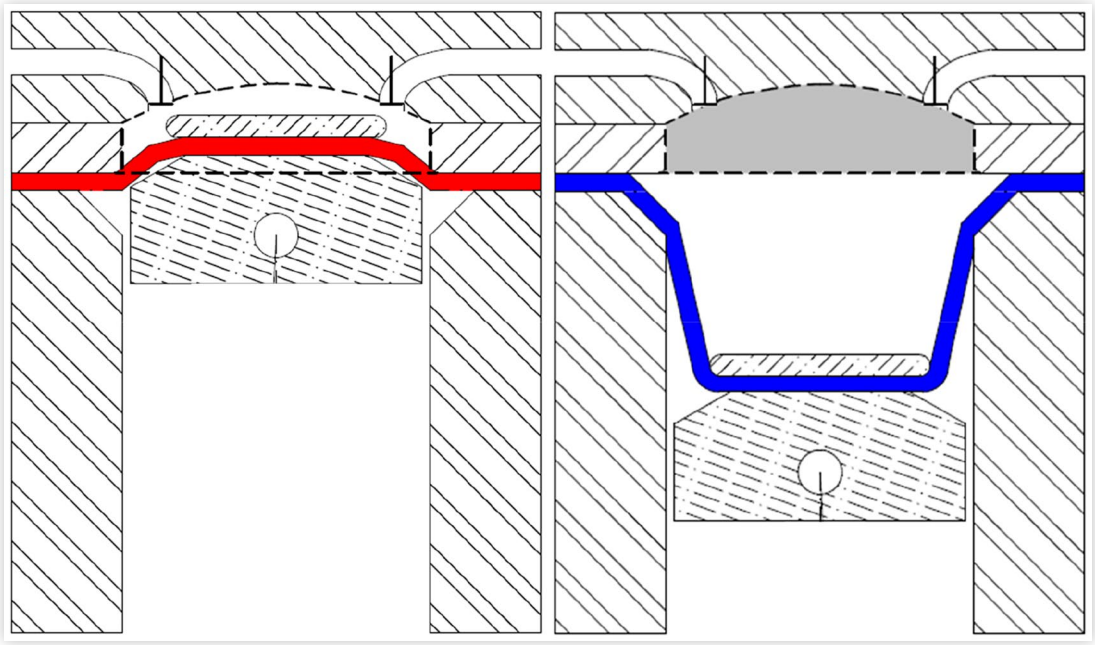

FIGURE 7 Cross-sectional view of the prototype engine cylinder total volume 3D model, with the swept volume in dark gray, the clearance volume in yellow, and the outlines of simplified swept volumes of the upper (red) and lower (blue) truncated cones.

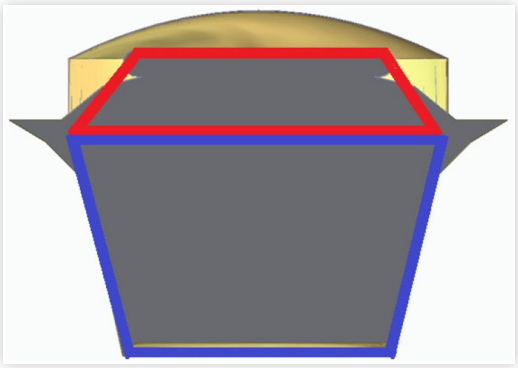

the engine cycle can be estimated geometrically. These calculations help extrapolate the membrane's displacement at specific points of the cycle and assess how it would respond to additional stresses imposed by cylinder pressures.

Figure 9 illustrates the calculation scheme for membrane displacement.

The membrane's strain is defined by the displacement from *L*1 to *L*2, while the pressure-induced expansion to *L*3 depends on overcoming internal stresses. These relationships are essential for modeling the membrane's dynamic shape and its effect on cylinder volume.

2.3.3. Expansion of the Membrane due to Internal Pressure

To model pressure-induced membrane deformation, the membrane is again approximated as a truncated cone, with the upper radius R_{Upper} equal to the cylinder bore and the lower radius R_{Lower} equal to the clamping disk radius. The cone height h_{exp} is the vertical distance from the disk at BDC to the point where the membrane is in a neutral plane (Figure 10). As the clamping disk radius R_{Lower} is smaller than the cylinder bore R_{Upper} we conclude that the membrane can only expand toward the cylinder wall starting from the disk, as indicated in Figure 9 by *L*3. Thus, we model the increase in volume as the increase of R_{Lower} incrementally for every CAD.

The maximum expanded radius R_{exp} can be derived by rearranging the truncated cone volume formula in Equation 5:

$$R_{\exp} = \frac{\sqrt{3}\cdot\sqrt{\pi}\cdot\sqrt{4\cdot V_{free}\cdot h_{\exp} - \pi\cdot h_{\exp}^2 R_{upper}^2} - \pi\cdot h_{\exp}\cdot R_{upper}}{2\cdot\pi\cdot h_{\exp}} \tag{5}$$

where

R_{exp} is the lower radius after expansion m;
V_{free} is the free volume between the membrane and combustion chamber m^3;
h_{exp} is the height of the expansion zone m;
R_{upper} is the upper radius of the constructed cone m.

As the pressure builds up in the combustion chamber, the membrane acts as a thin-walled pressure vessel, and thus the expansion of the wall can be modeled accordingly. Using Roark's formulas for stress and strain in Equations 6 and 7, the displacement of a conical pressure vessel wall under pressure can be described [48]:

$$\Delta R = \frac{p\cdot R_{lower}^2}{E_{tens}\cdot t\cdot\cos\alpha_{cone}}\cdot\left(1-\frac{\upsilon}{2}\right) \tag{6}$$

$$p_{\exp} = -\frac{E_{tens}\cdot t\cdot\Delta R_{\exp}\cdot\cos\alpha_{cone}}{R_{lower}^2\cdot\left(\frac{\upsilon}{2}-1\right)} \tag{7}$$

where

ΔR is the difference of the lower radius before and after stretching,
p is the internal pressure Pa,
R_{lower} is the initial radius of the constructed cone m,
E_{tens} is the modulus of the material under tension MPa,
t is the thickness of the stretched material m,
υ is the Poisson's ratio of the material,
α_{cone} is the slant angle of the constructed cone °,
p_{exp} is the pressure that induced the given expansion Pa.

In this model, expansion is limited by the membrane contacting the cylinder wall. The pressure range P_{exp} in Equation 8 required to induce this change is bounded between a minimum pressure P_{min} and a peak pressure P_{max}, beyond which no further expansion occurs.

TABLE 2 Membrane engine parameters.

Strokes	4	Connection rod length	84.8 mm
Cylinder	1	Crankshaft radius	27 mm
Engine power	***Not measured***	Displacement volume	154.10 cm^3
Speed	***Not measured***	Clearance volume	26.91 cm^3
Fuel supply system	Carburetor	Expandable volume	31.99 cm^3
Ignition system	Magneto spark ignition	Total volume (unexpanded)	181 cm3
Bore	70.00 mm	Total volume (expanded)	(max) 212.99 cm^3
Stroke	54.00 mm	Compression ratio	6.7 ... 7.5

FIGURE 8 Total cylinder volume 3D models for membrane deformation geometries at bottom dead center (BDC): stretched truncated cone (left) and pressure-expanded domed cylinder (right).

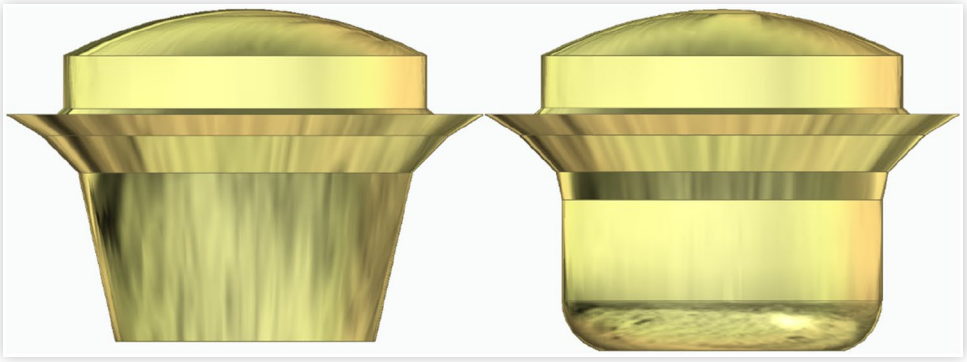

$$p_{exp} = \Delta p = p_{max} - p_{min} \quad (8)$$

Although the membrane is stretched up to 500% at BDC, most of the operating cycle occurs near the mid-range of displacement. For modeling purposes, a single tensile modulus value corresponding to the highest stress is used. This simplification is justified by the approximately linear behavior of elastomers in the central region of their stress–strain curve. This assumption is supported by both experimental data and literature on hyperelastic material modeling, which confirms that isotropic rubber-like materials behave nearly linearly under moderate strain conditions [49, 50].

Importantly, the model was constructed conservatively by using the tensile modulus measured at 500% elongation, which corresponds to the stiffest behavior of the membrane material. As a result, the calculated pressure-induced volume change is likely underestimated. In real operating conditions, the membrane is not always in its fully stretched position, and elevated temperatures during combustion are expected to increase the elasticity of the material, making it more responsive to pressure variations. Therefore, the actual deformation may be greater and occur at lower pressure thresholds than predicted by the current model.

Future experiments will focus on accurately measuring membrane displacement under dynamic conditions and refining the elastic modulus as a function of strain. This will enable more precise modeling of membrane behavior and geometry, supporting the development of advanced simulations beyond the initial proof-of-concept.

In ICE theory, the pressure rise in the cylinder caused by combustion is related to the amount of fuel burned. The

FIGURE 9 Calculation scheme for the displacement of membrane material while stretched ($L2$) and when expanded ($L3$) and while at original length ($L1$) with the lower (R_{Lower}) and upper (R_{Upper}) radius and height (h) of the truncated cone shown.

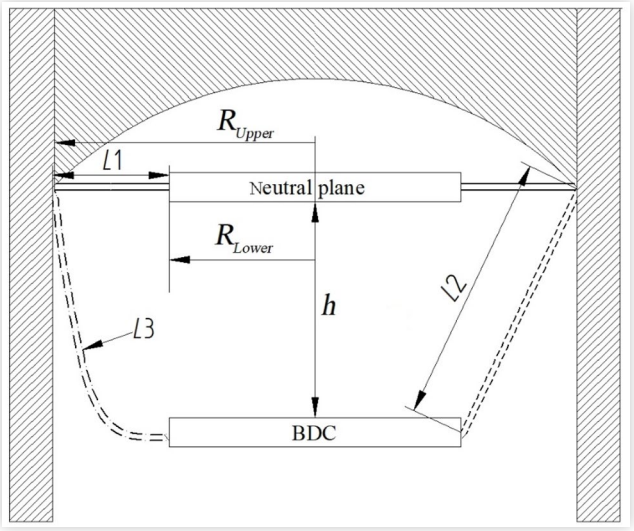

FIGURE 10 Calculation scheme for the expanded combustion chamber volume (R_{exp}) under pressure. Where R_n represents the incremental increase of the lower radius (and thus R_{exp}) due to pressure, V_{free} illustrates the free volume between the cylinder wall and membrane, and h_{exp} the height of the constructed cone.

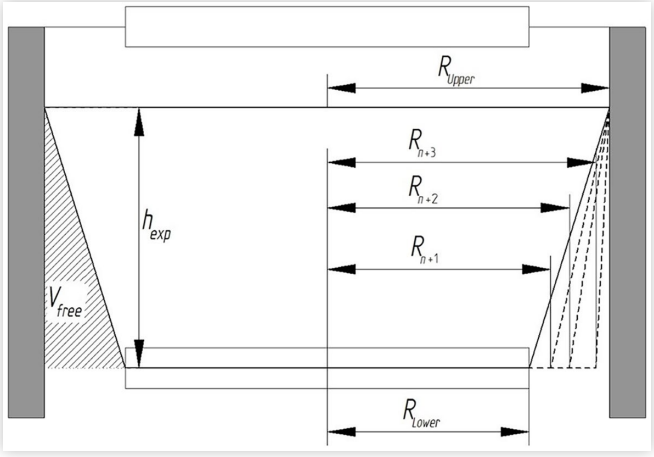

Wiebe function is commonly used to represent the mass fraction burned as a function of crankshaft angle [9, 51].

A similar approach can be applied here by adapting the Wiebe function to describe the increase in cylinder volume as a function of pressure. Equation 9 uses an exponential function that approaches unity, multiplied by the expandable volume V_{free}, and added to the instantaneous volume calculated from the geometric model. The resulting volume is the pressure-dependent cylinder volume of the membrane engine.

$$V_{pressure} = V_{free} \cdot \left\{ 1 - exp\left[-a \left(\frac{p_{cylinder} - p_{min}}{\Delta p} \right)^{m} \right] \right\} \quad (9)$$

where

$V_{pressure}$ is the volume increase of the combustion chamber due to pressure m^3,
V_{free} is the free volume between the membrane and combustion chamber m^3,
$P_{cylinder}$ is the instantaneous cylinder pressure Pa,
P_{min} is the minimum pressure during the cycle Pa,
Δp is the pressure difference of P_{min} and P_{max},
$exp(z)$ is the Euler's number raised to the power z (e^z),
a, m are the function shape constants.

The use of a Wiebe function–like exponential form in Equation 9 is intended as a pragmatic approximation to describe membrane expansion in response to pressure. While the function shape is inspired by combustion modeling, it does not represent a physically derived deformation law. Instead, it serves as an empirical fit to enable dynamic volume estimation based on measured cylinder pressure. This approach was chosen due to the lack of established theory for elastic combustion chamber boundaries and the absence of direct volume measurements during engine operation.

The constants a and m are used to adjust the shape of the function to fit experimental data, as is common in the original Wiebe function [9, 51, 52]. In this context, a controls the sensitivity of volume increase with respect to pressure—higher values of a result in a steeper response. Conversely, m affects the curvature of the function—higher values of m reduce the influence of pressure on volume change. These parameters were selected based on typical values used in combustion analysis and are not calibrated to membrane-specific deformation data. Future experiments will focus on collecting such data to determine optimal values for this application.

It is acknowledged that pressure and volume are thermodynamically coupled, and that using pressure as both input and validation introduces limitations. However, in the current setup, pressure is the only available dynamic variable that can be measured with sufficient resolution to approximate membrane behavior. The model should therefore be interpreted as a simplified empirical construct, designed to support concept validation and experimental interpretation, rather than as a predictive or physically complete representation.

This final model in Equation 10 captures both geometric and pressure-induced volume changes in the membrane engine:

$$V(\theta) = V_c + \frac{\pi \cdot h_1}{12} \cdot \left(d^2 + d \cdot B + B^2 \right) - \frac{\pi \cdot \left(h_1 - a + \sqrt{l^2 - a^2 \cdot \sin\theta^2} + a \cdot \cos\theta - \sqrt{l^2} \right)}{12} \cdot \left(d^2 + d \cdot B + B^2 \right) + V_{pressure} \quad (10)$$

where

$V(\theta)$ is the membrane engine cylinder volume m^3;
V_c is the combustion chamber volume m^3;
h_1 is the height of the upper cone at TDC m;
B is the upper diameter of the membrane (cylinder bore) m;
d is the lower diameter of the membrane (membrane fastening disk) m;
a is the crank radius m;
l is the connecting rod length m;
θ is the crankshaft position °;
$V_{pressure}$ is the volume increase of the combustion chamber due to pressure m^3.

Although the model simplifies the actual membrane behavior, it still enables pressure-dependent volume estimation. This dynamic aspect is essential for analyzing experimental data and cannot be captured by conventional PE models that rely solely on crank angle.

2.4. Assessing the Developed Model through a Theoretical Compression Line

For pressure-dependent model validation, cylinder pressure was calculated using an isentropic compression and expansion model (Figure 11), This method allowed the integration of the pressure-dependent volume term, enabling assessment of whether membrane deformation is reflected in the results.

Using the prototype's geometry, volume–crank angle diagrams were generated (Figure 11). The first graph (Figures 11 and 12 in blue) assumes no membrane expansion under pressure. The second allows for expansion.

Since the prototype is based on a PE, the engine geometry and the guiding member (Figure 5) restricts membrane movement near TDC. To reflect this constraint in the pressure-dependent volume model, in the third case (Figure 12 black dashed line), the membrane was considered immobile during crank angle intervals from –50° to +50° CAD and from –310° to +310° CAD, where

FIGURE 11 Modeled isentropic compression curve for unexpanded (blue) and expanded (black) membranes.

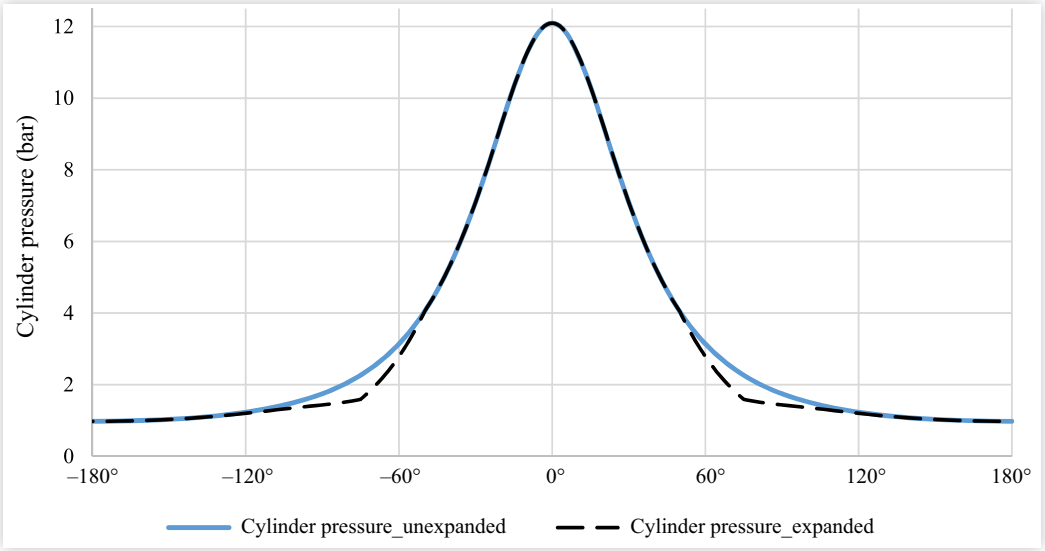

the elastic material is pressed against the guiding member (Figure 6, left). Since this limitation is specific to the current prototype and is expected to be eliminated in future designs, it was not included in the general model.

To avoid abrupt discontinuities in the volume–crank angle curve within the non-computable CAD range, the last two computable values on each side of the gap were used as an input to generate a smooth transition using exponential interpolation. This smoothing was implemented over a 24° transition zone preceding and following the undefined region, ensuring a gradual return of the membrane to a flat position. Because the actual membrane behavior in this range is unknown, a smooth transition was considered the most reasonable choice, preventing unrealistic sharp steps in the diagram that could distort subsequent calculations.

Although an isentropic process is idealized, the modeled graphs reveal how membrane expansion could alter pressure dynamics:

- During compression, pressure rise is delayed due to increased volume.
- The membrane's motion may also influence charge motion and combustion characteristics.
- In early combustion, membrane expansion increases chamber volume, potentially reducing pressure spikes and enabling a variable compression ratio.
- In later stages, membrane contraction may enhance combustion by directing flow toward the chamber center and reducing crevice effects.
- Additionally, the stored elastic energy may accelerate exhaust gas expulsion.

FIGURE 12 Modeled volume–crank angle diagrams of the unexpanded (blue) and expanded (gray) cylinder volumes, based on a theoretical compression curve.

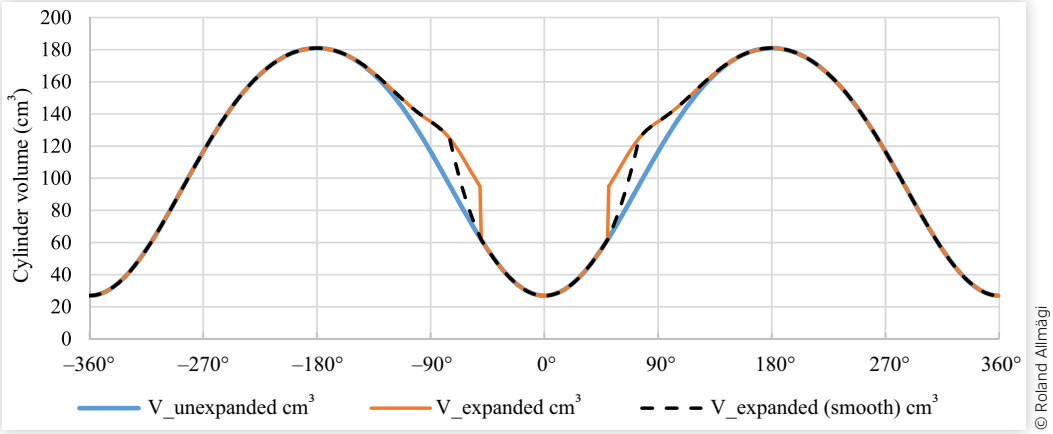

FIGURE 13 Engine test bench with the unmodified piston engine mounted.

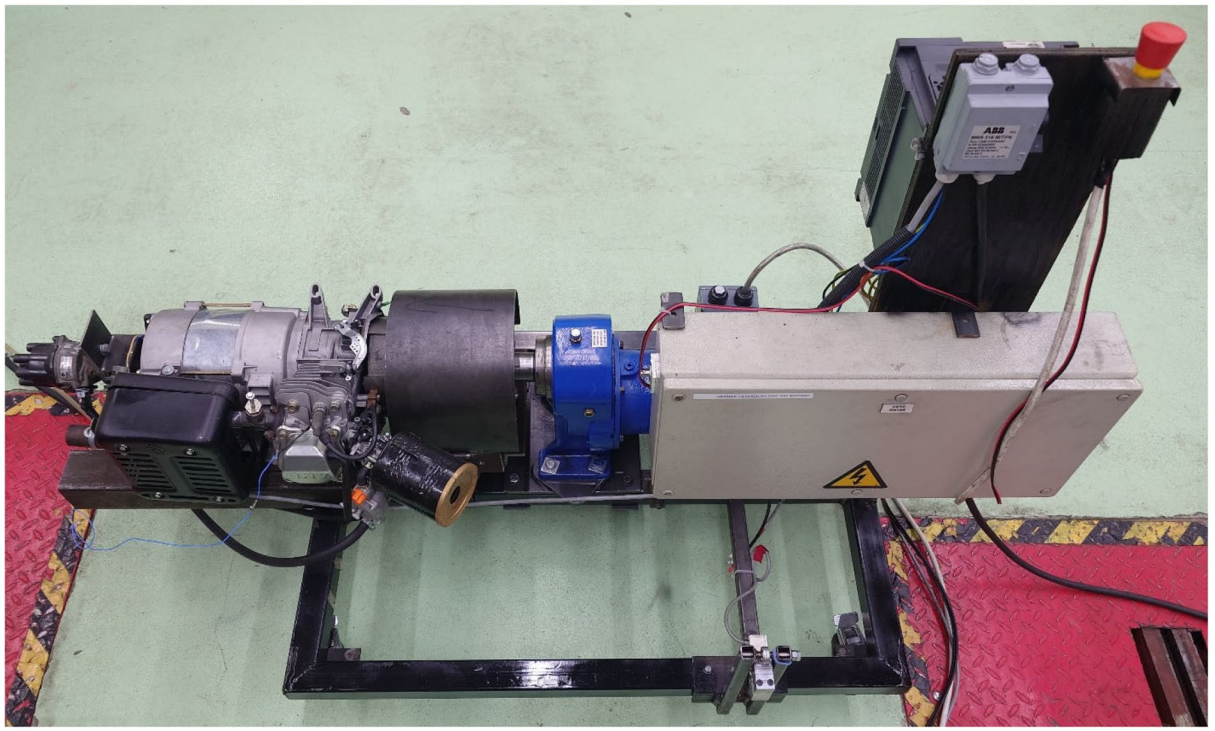

To validate these hypotheses and the model itself, comparative testing with a conventional PE is essential.

2.5. Engine Test Setup

To validate the membrane engine concept and the derived model, preliminary tests were conducted on a custom-built test bench for small engines (Figure 13). The prototype was tested under steady-state conditions at 750 rpm, with measurements taken for engine speed, torque, and cylinder pressure. For comparison, both the unmodified PE and the membrane prototype were tested under identical conditions.

Engine load was adjusted via carburetor throttle position to match torque values and monitored in real time using the AVL IndiCom interface. Factory settings for ignition timing and valve actuation were retained.

A 9 kW inverter-controlled induction motor (IM), coupled via a 4.06:1 gear reduction, maintained constant engine speed. Torque was measured using a force transducer mounted on a lever arm attached to the IM stator (Figure 14). The torque measured at the transducer was multiplied by the gear ratio to estimate the crankshaft torque.

Drivetrain friction losses were determined with the ICE decoupled and the gearset warmed up. These losses were measured as 2.05 Nm at 750 rpm and used as a static correction factor. It is acknowledged that actual losses under load may be higher, but this approximation was considered sufficient for initial validation.

Crankshaft speed and position were recorded using an optical sensor with 360 reference marks. Cylinder pressure was measured with an AVL GH 13Z-24 piezoelectric transducer mounted in the cylinder head. All signals were captured using an AVL 621 Indimodul data acquisition system and analyzed with AVL IndiCom and supplementary computational tools.

FIGURE 14 Engine torque measurement scheme.

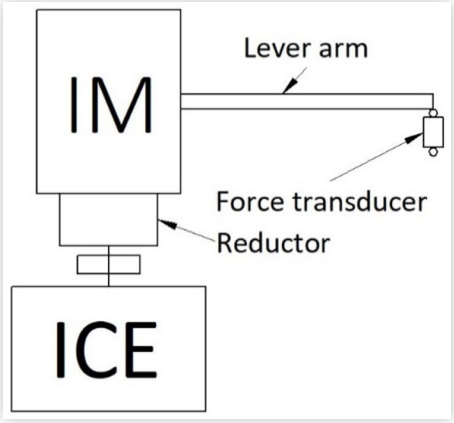

Details of the sensors and measurement equipment, including accuracy specifications, are provided in the supplementary materials (Table S.1).

The membrane used in the prototype was made from 5 mm thick natural rubber (NR). To verify its suitability, a tensile test was conducted according to ISO 37:2005, yielding a modulus of 0.37 MPa at 500% elongation. The required elongation in the assembled configuration was estimated to be at least 500%, which the material withstood without failure, as NR typically can withstand elongation up to 800% [53].

Although NR is not ideal for combustion environments [54], it was selected for its availability and superior elasticity to demonstrate the concept rather than to serve as a durable solution. Several alternative materials with higher thermal and chemical resistance were also tested, including neoprene, nitrile rubber, styrene–butadiene rubber, and silicone rubber. However, these materials exhibited insufficient elasticity for the required deformation range, making them unsuitable for the intended membrane function.

NR was therefore selected to demonstrate the concept, not as a final solution for combustion-grade durability.

2.6. Test Methodology

Engine tests were conducted under motored and fired conditions for both engines. This enabled comparison of mechanical losses, cylinder pressure, and torque distribution throughout the engine cycle.

Motored tests were performed with wide open throttle to minimize pumping losses. The carburetor was kept dry to avoid fuel vapor affecting the pressure trace. These tests provided baseline data for frictional losses and mechanical resistance.

For fired tests, the membrane engine was rotated by the test bench while the throttle valve was gradually opened. Combustion onset was monitored in real time using the AVL IndiCom interface. Once stable combustion was achieved, operating parameters were recorded. No predefined load points were used, as the goal was to establish a single point of stable operation. Later, similar conditions (engine speed and output torque) were recreated in the unmodified engine.

Since the AVL IndiCom software is primarily designed for conventional reciprocating engines, and the membrane engine exhibits non-standard behavior, all calculations related to IMEP and other metrics were performed outside the software. This allowed the research team to maintain full control over the data processing and ensure compatibility with the membrane engine's unique characteristics.

If the developed models prove suitable, future work will focus on integrating them into the software environment. For the current study, measured engine torque, cylinder pressure, and crankshaft position were used as the primary metrics for comparison.

After multiple test runs, one representative dataset was selected for analysis. Each dataset contained at least 100 engine cycles, which was deemed sufficient to validate whether the membrane engine can function as an ICE. If the proof-of-concept is successful, a more optimized design will be developed for extended testing and feasibility evaluation.

2.7. Motored Engine Torque

During testing, engine torque was recorded for each crank angle degree using a force transducer. The values presented here are crankshaft torque values corrected for drivetrain resistance. Raw measurements, including standard deviation error bars, are provided in the supplementary materials (Figure S.1).

Motored torque measurements (Figure 15) were used to compare frictional losses between the piston and membrane engines. Since both engines share the same base design, observed differences are attributed to the piston versus membrane configuration. Negative torque values indicate input work; positive values represent work produced by the engine.

The membrane engine showed higher overall resistance. This is likely because, during motored operation, the membrane does not significantly expand after stretching and therefore does not store elastic energy to offset the input work. This higher input work in this mode does not contradict the hypothesis that the membrane could reduce reciprocating losses under fired conditions.

Material properties, membrane thickness, and geometry (e.g., cylinder bore and clamping disk dimensions) strongly influence torque behavior. In this prototype, the bore-to-stroke ratio was not optimized for membrane stretchability.

Torque trends reveal further insights. During the intake stroke (–360 to –180 CAD), energy is used to stretch the membrane, which is partially recovered as it returns toward TDC (between –90 and 0 CAD). At the beginning of the intake stroke, near TDC, elastic forces are relatively small and may even be lower than piston friction. Near BDC, the elastic resistance of the membrane becomes significantly larger than the relatively constant frictional resistance of the PE. This difference in force balance helps explain the parabolic shape of the torque curve: the elastic energy stored in the membrane results in an almost symmetric rise after BDC. The peak is not as high as before, since additional energy is needed to flex the membrane past the neutral plane toward its uppermost position (Figure 6).

In contrast, PE's resistance stems mainly from sliding friction and intake flow losses, where the energy dissipates as heat and cannot be recovered in the next cycle, unlike the elastic energy stored in the membrane.

During the power stroke (0–180 CAD), gas pressure assists both engines, but in the membrane engine, stretching opposes motion, resulting in a flatter torque

FIGURE 15 Corrected motored torque of the Piston (blue) and membrane engine (black).

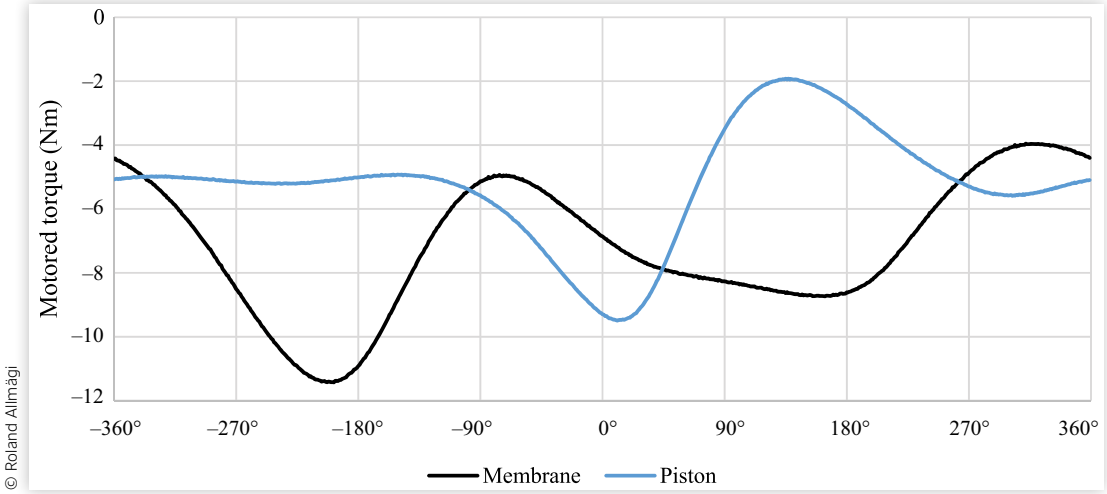

curve. In the exhaust stroke (180–360 CAD), the membrane's stored energy aids gas expulsion, producing higher torque values than the PE, supporting the hypothesis that an elastic membrane can enhance exhaust flow.

Overall, the torque amplitude (i.e., the difference between peak positive and negative values) is similar for both engines. This suggests that while the membrane engine introduces higher resistance in motored mode, its dynamic behavior may offer advantages under fired conditions.

2.8. Fired Engine Torque

Following successful motored testing, the membrane engine was operated under fired conditions. As before, torque values were recorded directly from the force transducer and later corrected by applying the gearbox ratio and adjusting for drivetrain resistance. Raw measurement values without these corrections, including standard deviation error bars, are provided in Figure S.2 in the supplementary materials.

Analysis of the graph reveals the following observations.

First, the PE curve exhibits a minor irregularity just after 180 CAD, which is most likely due to a single-point data acquisition error and does not reflect an actual abrupt change in engine torque; therefore, it can be disregarded in the overall analysis.

Second, despite generally lower torque values, the membrane engine shows a more pronounced positive torque spike after combustion. This is likely due to the membrane's elastic recoil aiding the upward motion during compression and influencing combustion dynamics. This effect is visible between –30 and 150 CAD, where the membrane engine curve rises more steeply than the PE's.

Third, the membrane engine produces more positive torque between 90 and 210 CAD, even though average torque values are –1.25 Nm (membrane) and –0.22 Nm (piston). This suggests that while both engines perform similar amounts of positive mechanical work, the membrane engine distributes forces differently across the cycle.

Calculated brake torque values later revealed that the engine's power output was insufficient to overcome the test bench's resistance. Due to the 4.06:1 gear ratio, the ICE needed to deliver approximately four times more torque to offset the inertia and friction of the IM and gearset before any positive torque could be registered. This explains the predominantly negative torque values observed in Figure 16.

In a different configuration, or if decoupled from the test bench, the engines would likely have been capable of operating independently and generating positive work output, even at such a narrow throttle opening. Given the membrane engine's higher mechanical resistance, mainly due to prototype geometry, it likely generates more positive work to achieve comparable output torque.

Further testing with optimized geometry and materials is needed. Additionally, testing under varied speeds and loads, along with electronically controlled ignition and fueling, would improve control and performance evaluation.

2.9. Limitations of the Prototype Engine

2.9.1. Material The membrane used in the prototype engine was made of NR, selected primarily for its high elasticity and local availability. Although NR is not suitable for long-term operation in combustion environments due to its limited thermal and chemical resistance, it was chosen to demonstrate the feasibility of the membrane engine concept. The material's ability to withstand

FIGURE 16 Fired torque of the piston (blue) and membrane engine (black).

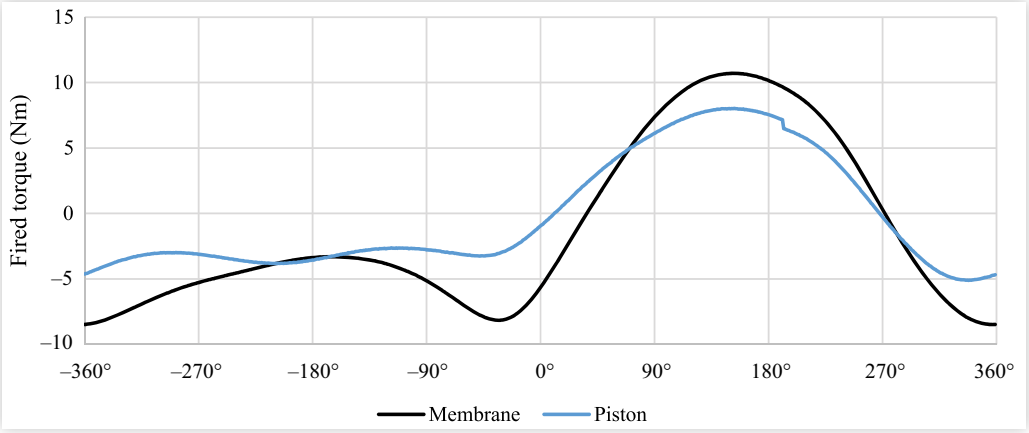

elongation up to 800% made it one of the few candidates capable of enduring the required deformation range.

To verify its suitability, a dry endurance test was conducted on a specialized test rig (Figure 3). The membrane was subjected to repeated stretching cycles, simulating the mechanical stresses encountered during engine operation. The results confirmed that NR could withstand the necessary test cycles without failure, validating its use for motored testing.

However, the tests revealed a wear pattern forming around the edge of the clamping disks (Figure 17). This wear was mitigated by applying lubricant between the membrane and the clamping surfaces. In the actual engine, lubrication is provided by oil from the crankcase, which is expected to reduce friction and wear severity.

FIGURE 17 Clamping disk wear pattern on the membrane material after motored tests. (The pink hue is due to a red lubricant used between the membrane and disk to aid assembly and reduce friction during testing.)

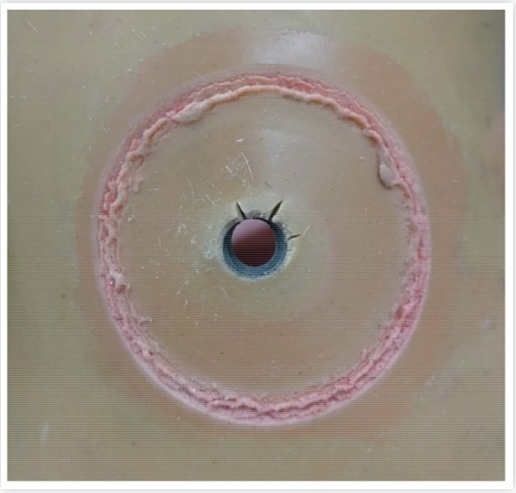

Therefore, the observed wear was assessed as minimal under operating conditions.

After motored tests were successful in the sense that torque and cylinder pressure could be measured for a reasonable amount of engine cycles and the prototype validated fit for reciprocating engine use, the same material was used for the first fired tests. While knowing the limitations of the material in handling high temperatures, contact with fuels, and other harsh conditions, the team still could get data from the fired engine, and no other material was sourced for the preliminary fired tests. Fired tests typically lasted around 15 min. The membrane failed due to localized thinning, which was caused either by thermal degradation that burned the material thinner (Figure 18 left) or by mechanical wear near the central mounting area.

The longevity of the membrane was strongly influenced by combustion quality. When the engine started promptly, fuel did not soak into the rubber and the heat softened the material, improving its flexibility. In contrast, delayed ignition led to dry friction and excessive fuel accumulation, which caused the membrane to fail more rapidly (Figure 18 right).

To improve durability in future iterations, a barrier between the elastic membrane and the combustion chamber is necessary. One possible solution is a metallic shield mounted on top of the clamping disk in a way that does not restrict membrane movement.

In addition to thermal and chemical effects, engine speed also plays a critical role in membrane longevity. At higher engine speeds, the membrane has less time to deform under pressure, which may reduce the extent of pressure-induced volume expansion. The dynamic response of the membrane depends on its material properties, particularly elasticity and damping. As speed increases, inertial forces and viscoelastic effects may limit the membrane's ability to follow rapid pressure changes, potentially resulting in a lower effective expansion ratio. Additionally, at very high speeds, the membrane may no

FIGURE 18 Membrane material after extended fired operation (left) and following premature failure (right).

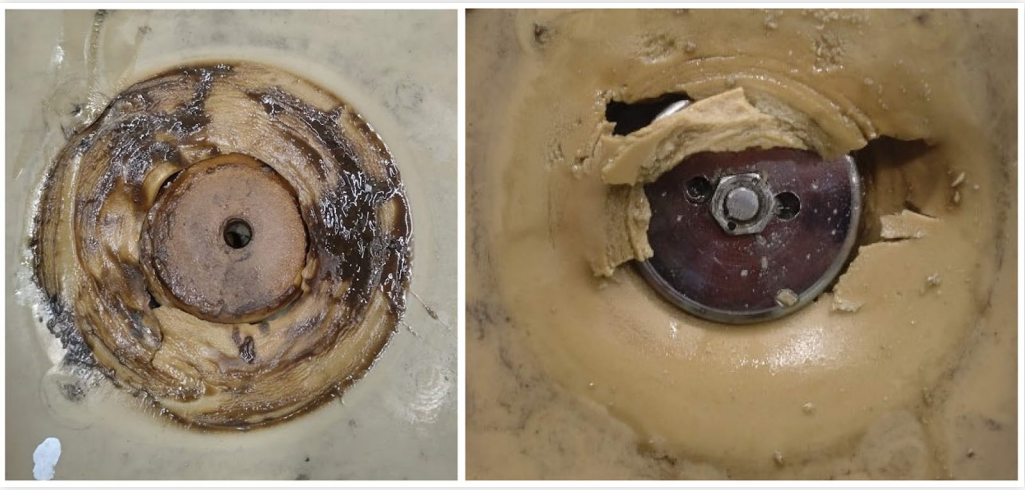

longer have sufficient time to stretch elastically, which could lead to mechanical failure due to tearing or detachment. This sets a practical upper limit for engine speed, beyond which the membrane material must be specifically engineered to withstand rapid cyclic deformation.

It is acknowledged that membrane material selection is and will remain a critical factor for the viability of this concept. However, the primary objective at this stage was to determine whether the membrane engine principle itself is feasible. Developing an optimized material before validating the concept would have been inefficient, as a negative outcome would render such material development irrelevant. Future work will therefore focus on addressing material limitations once the fundamental concept has been confirmed.

One alternative approach to this concept could be in waste heat recovery applications, where the hot exhaust gases of a PE could be routed to a membrane-fitted expansion chamber. With the added benefits of water injection, this could increase the efficiency of conventional PEs without the danger of engine oil fouling thanks to the superior sealing ability of the membrane. This configuration could be particularly relevant in multi-stage expansion systems, such as those found in five-stroke engine architectures, where the exhaust energy is partially recovered in a secondary expansion cylinder [50–52].

2.9.2. Engine Geometry The cylinder head of the original engine had to be modified to enable clamping of the membrane at the outer edges. This required relocating the valve pushrods outside the engine case. While this added mechanical complexity, it did not negatively affect valve lift or timing. As a side effect, the crankcase ventilation was sealed by the clamping plates, resulting in pulsating pressure within the crankcase. This pressure was vented to the atmosphere through a 6 mm pneumatic tube fitted to an opening in the case. An oil catch can was installed to minimize oil loss. However, due to the narrow diameter of the vent, crankcase back pressure may have restricted membrane movement.

As a sidenote, one of the claims found in a reviewed patent was confirmed: the crankcase can, with the aid of one-way valves, be used to pump fluid.

The cylinder bore of the modified engine was also too narrow, and the size of the reciprocating clamping disk was almost as big as the bore (50 mm). This limited the amount of flexible membrane material available for deformation. Future prototypes should incorporate a larger cylinder bore and potentially a shorter stroke. The size of the clamping disk cannot be reduced, as the flexible material was observed to detach in some cases. A different approach to fastening the membrane could also reduce friction between the disk and the membrane (Figure 17).

2.9.3. Fuel and Ignition System The original carburetor was designed for optimal flow at 3000 rpm, which resulted in suboptimal fueling at lower engine speeds. Additionally, the engine's startup procedure introduced challenges even with a closed throttle. Before ignition could occur, the engine had to be accelerated to 750 rpm using the test bench. Only then could the throttle gradually be opened to find a stable operating point. Although repeated tests helped identify this position more reliably, the initial startup still resulted in excessive fuel entering the cylinder before combustion began. This led to fuel soaking into the membrane and contributed to premature wear.

The most stable combustion and longest test runs were achieved with a narrow throttle opening. However, this limited engine output and caused the engine to be overpowered by the test bench. Opening the throttle further allowed combustion to continue but introduced

instability, producing noisy data that was unsuitable for analysis. Additionally, the IndiCom software interpreted abrupt pressure fluctuations as errors or knocks and terminated data recording.

Future tests should employ electronic fuel injection to deliver fuel only when required and with greater precision. Similarly, an electronic ignition system would enable real-time adjustment during operation, improving control and performance evaluation.

2.9.4. Summary and Outlook The prototype membrane engine was successfully tested under motored and fired conditions, demonstrating that the concept can be physically implemented and operated. The tests provided valuable insights into membrane behavior, combustion dynamics, and mechanical integration. Several limitations were identified, including material degradation, geometric constraints, and control system inflexibility. These issues are not fundamental flaws but rather development challenges that can be addressed in future iterations.

Importantly, the goal of this study was not to prove feasibility in terms of durability or efficiency, but to validate the core concept of a membrane-based reciprocating engine. In that regard, the prototype fulfilled its purpose. Future work will focus on improving membrane materials, refining engine geometry, and implementing electronic control systems to enable more precise and repeatable testing. The concept also shows potential for auxiliary applications, such as waste heat recovery, where membrane-based expansion could complement conventional PEs [8, 45, 49].

3. Results and Discussion

3.1. Cylinder Volume Calculation Based on Measured Pressure

Following engine testing, the actual cylinder pressure during the membrane engine working cycle was measured and used to calculate the engine volume throughout the cycle, as shown in Figure 19. To highlight the effect of membrane expansion, the graph of the expanded cylinder volume is overlaid on the unexpanded volume using a dashed line.

The modeled volume curve was constructed using constants a = 5 and m = 2, which are commonly used in Wiebe function applications to describe the burned fuel fraction in conventional engines [9, 47, 53]. These values provide a reasonable starting point when applying the original Wiebe function in combustion modeling. Even in traditional applications, the constants a and m are typically adjusted to fit measured pressure curves for each specific engine. Since comparative data is not yet available for the membrane engine, the standard values were adopted to enable initial analysis. This approach reflects the assumption that pressure rise is related to the amount of fuel burned, similar to conventional combustion theory.

The modeled volume graph (Figure 19) suggests that during combustion (60 … 180 CAD), the cylinder volume may exceed that of the compression phase (–180 … –60 CAD), indicating a variable compression and expansion ratio, with expansion being greater.

FIGURE 19 Modeled unexpanded membrane engine cylinder volume (blue) with the theoretically larger volume after expansion (black dashed) during the four-stroke working cycle with measured cylinder pressure (gray).

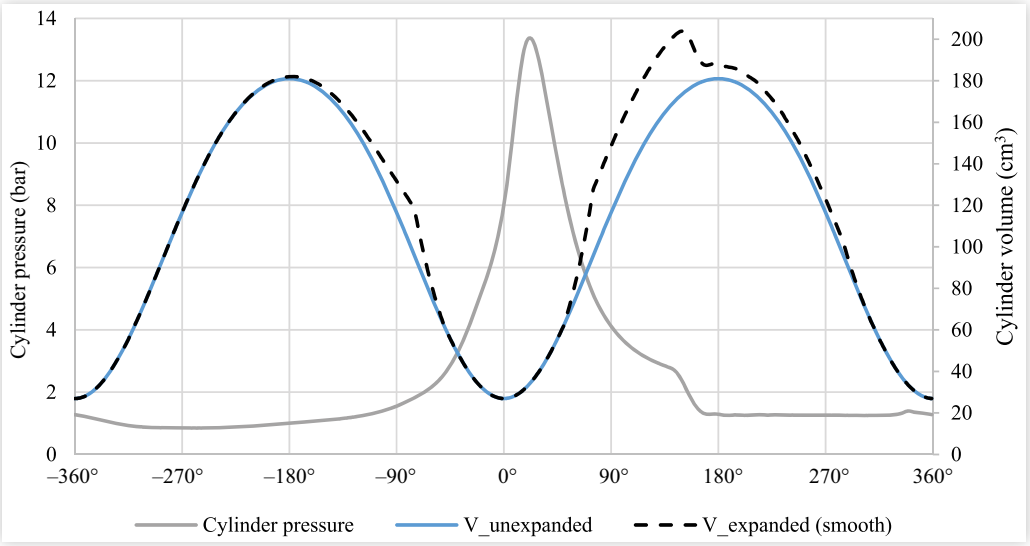

3.2. Exhaust Stroke Blowdown

Cylinder pressure traces confirmed that the membrane's stored elastic energy enhances exhaust gas flow. Despite identical valve timing and geometry, the membrane engine exhibited a steeper pressure drop after exhaust valve opening compared to the PE (Figure 20).

Given that both engines shared identical cylinder heads, valve lift, and timing, and operated at the same speed, the intake and exhaust flow conditions were assumed equivalent. Despite this, the membrane engine (black curve) exhibited a faster pressure drop than the PE (blue curve) and a lower pressure at the end of the exhaust stroke. This was observed even when the latter had a higher initial pressure during some tests. This suggests that the membrane, having expanded under combustion pressure, contracts as pressure falls, actively assisting blowdown (highlighted in Figure 20 in the lower graph).

According to the modeled membrane expansion (Figure 19), this effect persists until ~180 CAD, while the exhaust valve opens around 111 CAD, indicating that the rapidly contracting membrane contributes to exhaust flow over an extended duration.

Based on Figures 19 and 20, there is no doubt that the membrane expands under pressure; the question lies in the exact extent and timing of this expansion. Different pressure levels and corresponding membrane deformation are real and expected phenomena. Further research is needed to accurately determine when and to what degree the membrane expands, and to refine the model accordingly. At this stage, it remains uncertain whether the current approach fully captures the actual behavior.

Lastly, a small pressure rise was observed just before TDC on the intake stroke (~340 CAD). While the cause remains uncertain, it may result from rapid gas flow, valve–membrane interaction during overlap, or pressure wave reflections in the sensor tube. Cylinder pressure graphs with standard deviation error bars are provided in the supplementary materials (Figures S.3 and S.4).

3.3. p–V Diagram Analysis

To evaluate the membrane engine's thermodynamic behavior, a pressure–volume diagram was constructed using measured cylinder pressure and the modeled volume data. The diagram compares the unexpanded

FIGURE 20 Indicated cylinder pressure and valve lift graph of the piston and membrane engine for the whole cycle (upper) and a close-up of the exhaust stroke (lower).

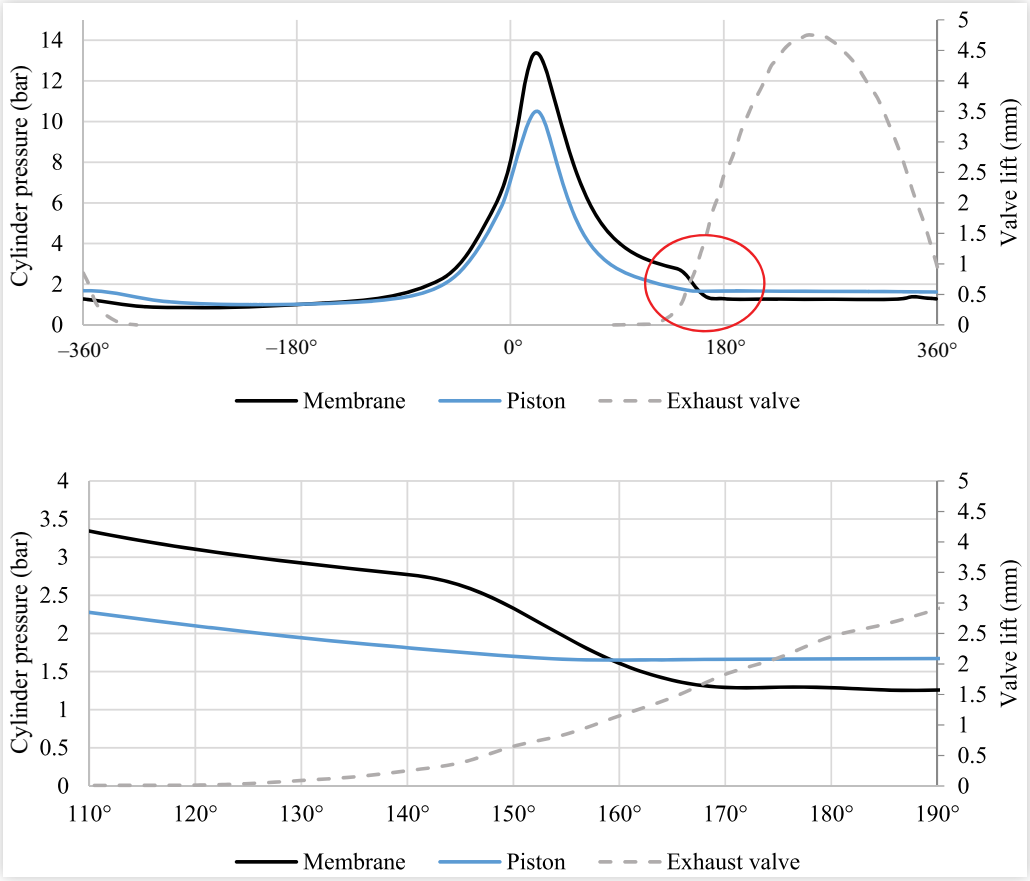

FIGURE 21 Modeled p–V diagram of the membrane engine expanded (black dotted) and unexpanded (blue).

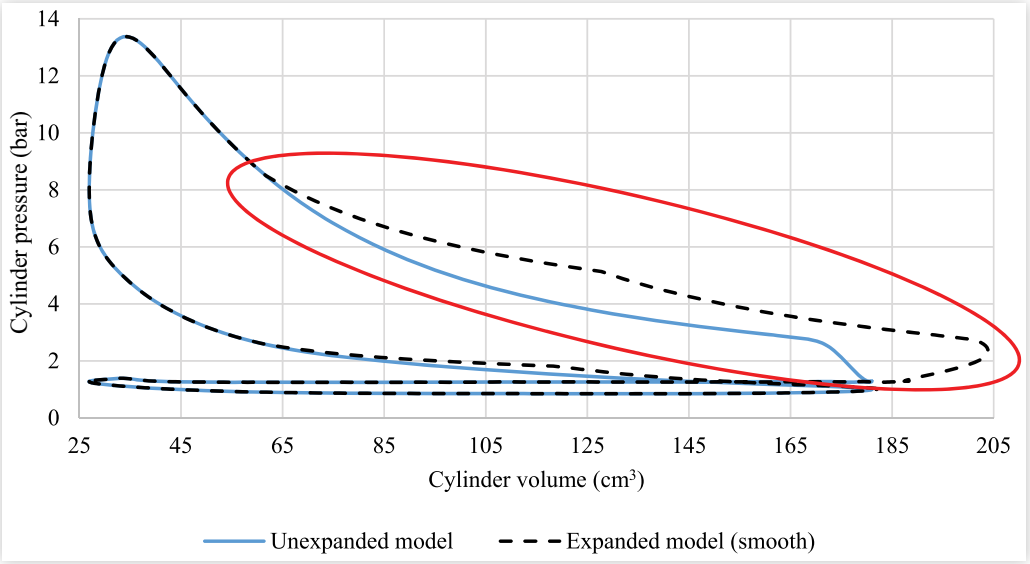

and expanded volume curves throughout the four-stroke cycle, highlighting the effect of membrane deformation on combustion chamber volume.

Initial analysis of the modeled p–V diagrams (Figure 21) shows that the area enclosed by the expanded membrane model (black dashed curve) is larger than that of the unexpanded model (blue curve), particularly during the combustion stroke (region highlighted with red circle). This suggests a potential for increased usable work output.

Comparing measured test data in Figure 20 with the modeled diagrams of Figures 19 and 21 supports the hypothesis that membrane expansion introduces a pressure-dependent, variable compression ratio.

Further testing is required to validate these findings and refine the model to better reflect real-time volume changes during engine operation.

3.4. Indicated Work per Cycle

To evaluate the membrane engine's performance, the indicated work per cycle was calculated using measured cylinder pressure and the modeled volume data [9]. The calculation was performed for both the unexpanded and expanded volume models to assess the influence of membrane deformation on work output.

Table 3 presents the calculated indicated work values for the PE and the prototype engine. Due to uncertainty in membrane behavior near TDC (–50 to 50 CAD), two cases were modeled: one with exponential smoothing applied to the pressure-dependent term and one without. This approach was taken to represent two limiting cases, with the actual behavior likely falling somewhere between these extremes.

In this work, gross indicated work includes compression and combustion strokes, while net indicated work accounts for the full cycle.

Table 3 shows that the membrane engine, particularly in the smoothed case, achieves higher gross and net indicated work, power output, and IMEP, while exhibiting lower pumping losses. Since indicated work is directly related to the change in cylinder volume and the elasticity of membrane enables more rapid volume transition, distinct processes can be observed in the graph below. The unsmoothed results are visualized in Figure 22, where the membrane engine (black line) shows distinct spikes in indicated work, corresponding to rapid volume changes during membrane expansion, stretching, and contraction (Figure 19).

The spike near the uncomputable ranges of BTDC is influenced by the guiding member (Figure 5) and may represent a modeling artifact.

The spike before 180 CAD correlates to a sudden volume change during exhaust gas blowdown.

Although peak combustion work is lower in the membrane engine (0–180 CAD), reduced work during compression and exhaust suggests that stored elastic energy aids in returning the membrane toward TDC. This trend is reflected in both the graph and the numerical data (Table 3), indicating a potential reduction in pumping work for the membrane engine. This suggests that membrane deformation under pressure contributes positively to the engine's thermodynamic performance. However, the absolute values remain preliminary due to the lack of calibration and the simplified nature of the membrane model.

It's important to note that these values are based solely on in-cylinder pressure and do not account for

TABLE 3 Comparison of indicated work per cycle of the piston and prototype engine based on test results.

	Piston engine	Expanded membrane engine (smooth)	Expanded membrane engine (w/o smoothing)
Work during intake (J)	24.41	13.99	13.98
Work during compression (J)	–39.04	–34.45	–27.96
Work during combustion (J)	87.5	105.92	86.16
Work during exhaust (J)	–34.25	–20.44	–19.67
Gross indicated work (J)	48.46	71.47	58.2
Net indicated work (J)	38.62	65.02	52.51
Gross indicated power (W)	302.88	446.69	363.75
Net indicated power (W)	241.38	406.38	328.19
Gross indicated mean effective pressure (bar)	2.33	4.04	3.29
Net indicated mean effective pressure (bar)	1.86	3.68	2.97
Pumping mean effective pressure (bar)	0.47	0.36	0.32

mechanical losses. If the engine geometry were optimized for membrane operation, the concept could theoretically achieve lower friction losses due to reduced sliding components.

3.5. Assessing the Model through Measured Data

At first glance, the modeling approach appears successful in the sense that it enables calculation of the engine's instantaneous volume throughout the cycle. Additionally, a more dynamic representation was achieved by incorporating pressure-dependent volume variation. However, the current model remains a gross simplification of the actual pressure-dependent behavior. The true shape and volume of the combustion chamber during operation are still unknown.

To address this limitation, future tests must aim to record the dynamic shape of the membrane using high-speed cameras and endoscopic imaging. This would provide direct visual data on membrane deformation under real operating conditions. Additionally, future tests will investigate membrane behavior at higher engine speeds to assess how deformation dynamics and pressure–volume coupling evolve under faster cycle conditions.

For more accurate modeling of pressure-dependent volume and membrane deformation, the same approach could be applied during combustion. Alternatively, a specialized test rig could be developed to simulate various crankshaft positions and pressure levels under both static and dynamic conditions—similar to how the truncated cone shape was derived using a variable-stroke rig (Figure 3). These tests would help validate whether the Wiebe function analogy is appropriate and determine which constants best fit the model to actual measured volume data.

FIGURE 22 Indicated work during the whole engine cycle for the membrane (black) and piston (blue) engine.

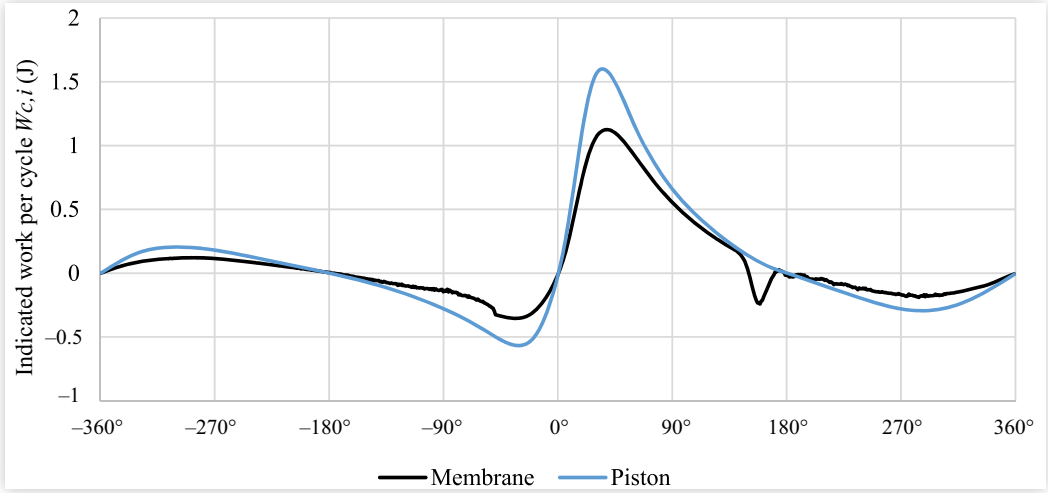

4. Conclusion

This study introduced the design, modeling, and experimental validation of a novel membrane engine concept, where a flexible elastic membrane replaces the traditional piston. Based on the literature, the membrane engine offers several potential advantages, including reduced mechanical friction, improved combustion chamber sealing, and lower heat losses. Its ability to flex and expand enables a variable compression ratio, which may enhance charge exchange efficiency and alter the cycle's torque distribution.

Mathematical models were developed to describe the membrane's geometry and pressure-dependent expansion. These were applied to a working prototype based on a modified single-cylinder spark-ignition engine and validated through motored and fired tests. The results confirmed several hypothesized benefits.

The pressure-dependent volume model showed that the membrane engine can achieve a variable compression ratio, potentially improving thermal efficiency. Experimental pressure traces revealed a steeper pressure drop during the exhaust stroke, supporting the hypothesis that elastic recoil enhances gas scavenging. Torque measurements also indicated a more pronounced positive torque spike after combustion, despite higher mechanical resistance during operation.

Torque analysis further showed that the membrane engine distributes forces differently throughout the cycle, suggesting it may influence combustion dynamics and gas flow. Although the prototype exhibited higher resistance due to suboptimal geometry and material choice, it still achieved comparable indicated work to the piston engine. This implies that even in a non-optimized state, the membrane engine can deliver similar mechanical output.

With further optimization—particularly in membrane materials, engine geometry, and the use of electronically controlled ignition and fueling, the membrane engine could show significant performance and efficiency gains. Future work should explore alternative materials, refine geometry to reduce resistance, and conduct long-term durability and emissions testing. Testing under varied speeds and loads will also be essential to fully characterize its performance and efficiency.

An additional concept for future development involves coupling a PE's exhaust system directly to the intake of a membrane engine, with both operating on a shared crankshaft. Variants of this concept are widely known in the literature as the split cycle [55–58], five-stroke [59–62], or six-stroke engines [22, 63].

In this configuration, the membrane engine would utilize the thermal energy of the exhaust gases for expansion work, effectively functioning as a waste heat recovery unit. This setup could extend membrane lifespan by reducing direct exposure to combustion temperatures and enabling the use of water injection without the risk of water entering the crankcase.

This research provides a foundational step toward a new class of reciprocating ICEs and demonstrates the potential feasibility of using elastic membranes as dynamic combustion chamber boundaries.

Acknowledgements

This research was supported by the Estonian Research Council under project EAG304, and by Neste Eesti AS. The authors gratefully acknowledge their contribution to enabling this work.

Declaration of AI-Assisted Technologies

Microsoft Copilot was used during the preparation of this manuscript to assist with grammar and phrasing improvements. All scientific content, including experimental design, data analysis, and literature review, was solely produced by the authors.

Contact Information

Roland Allmägi, corresponding author
Institute of Forestry and Engineering, Estonian University of Life Sciences, F. R. Kreutzwaldi 56, Tartu, Estonia
roland.allmagi@emu.ee

Abbreviations

a - Crankshaft radius
a - Function shape constant
ATDC - After top dead center
B - Cylinder bore
BDC - Bottom dead center
BTDC - Before top dead center
CAD - Crank angle degree
CR - Compression ratio
D - Lower diameter of truncated cone
d - Upper diameter of truncated cone
E_{tens} - Modulus of the membrane material
exp(z) - Euler's number (e^z)
h - Cone height
h_1 - Height of the upper cone at TDC
h_{exp} - Height of the expandable portion of the truncated cone
ICE - Internal combustion engine
IM - Induction motor

IMEP - indicated mean effective pressure
l - Connecting rod length
L1 - Original length of the membrane
L2 - Stretched length of the membrane
L3 - Expanded length of the membrane
m - Function shape constant
MEP - Mean effective pressure
NR - Natural rubber
PE - Piston engine
p - Internal pressure
$P_{cylinder}$ - Instantaneous cylinder pressure
p_{exp} - Pressure that induced the given membrane expansion
P_{max} - Peak pressure
P_{min} - Minimal cylinder pressure
R_{exp} - Lower radius of the truncated after expansion
R_{Lower} - Lower radius of the truncated cone
R_n - Incremental increase of the truncated cone lower radius due to pressure
R_{Upper} - Upper radius of the truncated cone
s - Piston/membrane stroke
t - Thickness of the membrane material
TDC - Top dead center
$V(\theta)$ - Instantaneous volume
V_c - Clearance volume/combustion chamber volume
V_{c1} - Upper truncated cone volume
V_{c2} - Lower truncated cone volume
V_d - Displacement volume
V_{exp} - Free volume between the cylinder wall and membrane
V_m - Volume of the conical membrane
$V_{pressure}$ - Volume increase of the combustion chamber due to pressure
α_{cone} - Slant angle of the constructed cone
Δp - Pressure difference of P_{min} and P_{max}
ΔR - Difference of the lower radius before and after stretching
θ - Crankshaft position
υ - Poisson ratio

References

1. Kalghatgi, G.T., "Developments in Internal Combustion Engines and Implications for Combustion Science and Future Transport Fuels," *Proceedings of the Combustion Institute* 35, no. 1 (2015): 101-115, doi:https://doi.org/10.1016/j.proci.2014.10.002.
2. Reitz, R.D., "Directions in Internal Combustion Engine Research," *Combustion and Flame* 160, no. 1 (2013): 1-8, doi:https://doi.org/10.1016/j.combustflame.2012.11.002.
3. Towoju, O.A. and Ishola, F.A., "A Case for the Internal Combustion Engine Powered Vehicle," *Energy Reports* 6 (2020): 315-321, doi:https://doi.org/10.1016/j.egyr.2019.11.082.
4. Leach, F., Kalghatgi, G., Stone, R., and Miles, P., "The Scope for Improving the Efficiency and Environmental Impact of Internal Combustion Engines," *Transportation Engineering* 1 (2020): 100005, doi:https://doi.org/10.1016/j.treng.2020.100005.
5. Sinigaglia, T., Eduardo Santos Martins, M., and Cezar Mairesse Siluk, J., "Technological Evolution of Internal Combustion Engine Vehicle: A Patent Data Analysis," *Applied Energy* 306 (2022): 118003, doi:https://doi.org/10.1016/j.apenergy.2021.118003.
6. Taylor, A.M.K.P., "Science Review of Internal Combustion Engines," *Energy Policy* 36, no. 12 (2008): 4657-4667, doi:https://doi.org/10.1016/j.enpol.2008.09.001.
7. Kimura, K., Sakai, H., Omura, T., and Takahashi, D., "Development of 50% Thermal Efficiency S.I. Engine to Contribute Realization of Carbon Neutrality," SAE Technical Paper 2023-01-0241 (2023), doi:https://doi.org/10.4271/2023-01-0241.
8. Sens, M., "Hybrid Powertrains with Dedicated Internal Combustion Engines are the Perfect Basis for Future Global Mobility Demands," *Transportation Engineering* 13 (2023): 100146, doi:https://doi.org/10.1016/j.treng.2022.100146.
9. Heywood, J.B., *Internal Combustion Engine Fundamentals*, 2nd ed. (New York: McGraw-Hill Education, 2018), ISBN:978-1-26-011611-3.
10. Fussey, P. and Limebeer, D., "Optimal Combustion Control with Application to Engine Design and Development," *Control Engineering Practice* 92 (2019): 104154, doi:https://doi.org/10.1016/j.conengprac.2019.104154.
11. Sprouse, C.E. III, "Review of Organic Rankine Cycles for Internal Combustion Engine Waste Heat Recovery: Latest Decade in Review," *Sustainability* 16, no. 5 (2024): 1924.
12. Kaushik, H., Rani, A., Sarna, N., and Rajak, R., "Analysis of Thermal Coating on Engine Performance Parameters & Fuel Economy of a Small Size NA Spark Ignition Engine," SAE Technical Paper 2021-28-0134 (2021), doi:https://doi.org/10.4271/2021-28-0134.
13. Jami, P., Pandey, K.K., and Sivalingam, M., "Performance and Emission Studies of a Dual-Fuel Diesel Engine in LHR Mode," *SAE Int. J. Adv. & Curr. Prac. in Mobility* 4, no. 5 (2022): 1943-1952, doi:https://doi.org/10.4271/2022-01-0514.
14. Kéromnès, A., Delaporte, B., Schmitz, G., and le Moyne, L., "Development and Validation of a 5 Stroke Engine for Range Extenders Application," *Energy Conversion and Management* 82 (2014): 259-267, doi:https://doi.org/10.1016/j.enconman.2014.03.025.
15. Lu, Y. and Pei, P., "Performance Evaluation of 4-Cylinder 5-Stroke Internal Combustion Engine," *Chinese Internal Combustion Engine Engineering* 36, no. 2 (2015): 18-24, doi:https://doi.org/10.13949/j.cnki.nrjgc.2015.02.004.

16. Zhu, S., Joo, N., Hollowell, J., Ha, K. et al., "Low Temperature Combustion Exploration with Negative Valve Overlap," SAE Technical Paper 2022-01-0452 (2022), doi:https://doi.org/10.4271/2022-01-0452.
17. Guan, J., Liu, J., Duan, X., Jia, D. et al., "Effect of the Novel Continuous Variable Compression Ratio (CVCR) Configuration Coupled with Spark Assisted Induced Ignition (SAII) Combustion Mode on the Performance Behavior of the Spark Ignition Engine," *Applied Thermal Engineering* 197 (2021): 117410, doi:https://doi.org/10.1016/j.applthermaleng.2021.117410.
18. Alkhaniya, A. and Kotiya, A., "Concept of Six Stroke Engine," *International Journal of Mechanical and Industrial Technology* 2, no. 2 (2015): 2-5.
19. Palanivendhan, M., Modi, H., and Bansal, G., "Five Stroke Internal Combustion Engine," *International Journal of Control Theory and Applications* 9, no. 13 (2016): 5855-5862.
20. Noga, M. and Sendyka, B., "New Design of the Five-Stroke SI Engine," *Journal of KONES* 20, no. 1 (2013): 239-246, doi:https://doi.org/10.5604/12314005.1136161.
21. Gregório, J.P. and Brójo, F.M., "Development of a 4 Stroke Spark Ignition Opposed Piston Engine," *Open Engineering* 8, no. 1 (2018): 337-343, doi:https://doi.org/10.1515/eng-2018-0039.
22. Arabaci, E., "Performance Analysis of a Novel Six-Stroke Otto Cycle Engine," *Thermal Science* 25, no. 3A (2021): 1719-1729, doi:https://doi.org/10.2298/TSCI190926144A.
23. Wittek, K., "Variables Verdichtungsverhältnis beim Verbrennungsmotor durch Ausnutzung der im Triebwerk wirksamen Kräfte," Doctoral Thesis, Rheinisch-Westfälischen Technischen Hochschule Aachen, 2006.
24. Shaik, A., Moorthi, N.S.V., and Rudramoorthy, R., "Variable Compression Ratio Engine: A Future Power Plant for Automobiles—An Overview," *Proceedings of the Institution of Mechanical Engineers, Part D: Journal of Automobile Engineering* 221, no. 9 (2007): 1159-1168, doi:https://doi.org/10.1243/09544070JAUTO573.
25. Hiyoshi, R., Aoyama, S., Takemura, S., Ushijima, K. et al., "A Study of a Multiple-Link Variable Compression Ratio System for Improving Engine Performance," SAE Technical Paper 2006-01-0616 (2006), doi:https://doi.org/10.4271/2006-01-0616.
26. Pandey, J.K. and Kumar, G.N., "Effect of Variable Compression Ratio and Equivalence Ratio on Performance, Combustion and Emission of Hydrogen Port Injection SI Engine," *Energy* 239 (2022): 122468, doi:https://doi.org/10.1016/j.energy.2021.122468.
27. López, J.J., García, A., Monsalve-Serrano, J., Cogo, V. et al., "Potential of a Two-Stage Variable Compression Ratio Downsized Spark Ignition Engine for Passenger Cars under Different Driving Conditions," *Energy Conversion and Management* 203 (2020): 112251, doi:https://doi.org/10.1016/j.enconman.2019.112251.
28. Littlefair, B., de la Cruz, M., Mills, R., Theodossiades, S. et al., "Lubrication of a Flexible Piston Skirt Conjunction Subjected to Thermo-Elastic Deformation: A Combined Numerical and Experimental Investigation," *Proceedings of the Institution of Mechanical Engineers, Part J: Journal of Engineering Tribology* 228, no. 1 (2014): 69-81, doi:https://doi.org/10.1177/1350650113499555.
29. Nikolakopoulos, P.G., Antonakakis, G., and Zavos, A., "On the Influence of Axial Cylinder Distortions on Lubricant Film and Friction Force of Top Piston Ring Conjunction Near to TDC," *Tribology - Materials, Surfaces and Interfaces* 16, no. 4 (2022): 356-372, doi:https://doi.org/10.1080/17515831.2022.2111045.
30. Menacer, B., Soualmia, A., Narayan, S., and Al-Lehaibi, M., "Impact Analysis of the Key Engine Parameters on Piston Lubrication and Friction Performance in Diesel Engines Using GT-SUITE Program," *Mechanics* 30, no. 3 (2024): 236-243, doi:https://doi.org/10.5755/J02.MECH.35251.
31. Bifeng, Y., Jiajun, Z., Bo, X., Gongyin, H. et al., "Friction and Wear Performance of Double-Bump Design of Piston Skirt Main Thrust Side," *International Journal of Automotive Technology* 21, no. 6 (2020): 1579-1586, doi:https://doi.org/10.1007/s12239-020-0148-y.
32. Menacer, B., Narayan, S., and Mahroogi, F.O., "Studying Hydrodynamic Friction in the Oil Ring/Cylinder Liner Contact of an Internal Combustion Engine," *Cogent Engineering* 10, no. 2 (2023): 1-14, doi:https://doi.org/10.1080/23311916.2023.2289261.
33. Romero, C., Ramírez, J., and Henao Castañeda, E., "Experimental Characterization of the Mechanical Loss Components of a Single-Cylinder Spark-Ignition Engine by Progressive Disassembly Method," SAE Technical Paper 2023-01-0416 (2023), doi:https://doi.org/10.4271/2023-01-0416.
34. Li, J., Zuo, Z., Jia, B., Feng, H. et al., "Comparative Analysis on Friction Characteristics between Free-Piston Engine Generator and Traditional Crankshaft Engine," *Energy Conversion and Management* 245 (2021): 114630, doi:https://doi.org/10.1016/j.enconman.2021.114630.
35. Lyu, X., Liang, X., Wang, Y., Wang, Y. et al., "Influence of Lubricants on Particulate Matter Emission from Internal Combustion Engines: A Review," *Fuel* 366 (2024): 131317.
36. Sanadhya, K., Nandgaonkar, M., and Aghav, Y., "Effect of Piston Secondary Motion on Lubricating Oil Consumption, Blow-by and Friction," *SAE Int. J. Adv. & Curr. Prac. in Mobility* 6, no. 6 (2024): 2901-2913, doi:https://doi.org/10.4271/2024-26-0259.
37. Gargate, S., Aher, R., Jacob, R., and Dambhare, S., "Estimation of Blow-by in Diesel Engine: Case Study of a Heavy Duty Diesel Engine," *International Journal of Emerging Engineering Research and Technology* 2, no. 2 (2014): 165-170.
38. George, S., Balla, S., and Gautam, M., "Effect of Diesel Soot Contaminated Oil on Engine Wear," *Wear* 262, no. 9–10 (2007): 1113-1122, doi:https://doi.org/10.1016/j.wear.2006.11.002.
39. Allmägi, R., Ilves, R., and Olt, J., "Comprehensive Review of Innovation in Piston Engine and Low Temperature

Combustion Technologies," *Transport* 39, no. 1 (2024): 86-113, doi:https://doi.org/10.3846/transport.2024.21333.

40. Joannes, H., "Verbrandingsmotor," NL8603054A, 1986, https://worldwide.espacenet.com/patent/search/family/019848921/publication/NL8603054A?q=pn%3DNL8603054A.
41. Breitgraf, H.J., "Kolbenloser Verbrennungsmotor (Membran-Motor)," DE000008800034U1, 1988, https://depatisnet.dpma.de/DepatisNet/depatisnet?action=pdf&docid=DE000003800099A1&xxxfull=1.
42. Meschendörfer, K., "Membran-Verbrennungsmotor," DE000008909481U1, 1989, https://depatisnet.dpma.de/DepatisNet/depatisnet?action=pdf&docid=DE000008909481U1&xxxfull=1.
43. Werding, H., "Scheibenmotor," DE102007009350A1, 2007.
44. Li, X., Chen, J., Wang, Z., Jia, X. et al., "A Non-Destructive Fault Diagnosis Method for a Diaphragm Compressor in the Hydrogen Refueling Station," *International Journal of Hydrogen Energy* 44, no. 44 (2019): 24301-24311, doi:https://doi.org/10.1016/j.ijhydene.2019.07.147.
45. Das, C.R., Ravishankar, C., Albert, S.K., Krishnan, S.A. et al., "Failure Analysis of Cold Worked AISI 301 SS Diaphragm of Gas Pump," *Engineering Failure Analysis* 92 (2018): 456-465, doi:https://doi.org/10.1016/j.engfailanal.2018.06.018.
46. Somhorst, J. and Oevermann, M., "Effects of Thermal Barrier Coating Porosity on Combustion and Heat Losses in a Light Duty Diesel Engine," *International Journal of Engine Research* 25, no. 5 (2024): 940-958, doi:https://doi.org/10.1177/14680874231215526.
47. Gautam, S.S., Singh, R., Vibhuti, A.S., Sangwan, G. et al., "Thermal Barrier Coatings for Internal Combustion Engines: A Review," *Materials Today: Proceedings* 51 (2021): 1554-1560, doi:https://doi.org/10.1016/J.MATPR.2021.10.371.
48. Young, W.C. and Budynas, R.G., *Roark's Formulas for Stress and Strain*, 7th ed. (New York: McGraw-Hill, 1989), ISBN:007072542X.
49. Dal, H., Açikgöz, K., and Badienia, Y., "On the Performance of Isotropic Hyperelastic Constitutive Models for Rubber-Like Materials: A State of the Art Review," *Applied Mechanics Reviews* 73, no. 2 (2021): 020802, doi:https://doi.org/10.1115/1.4050978.
50. INSTRON, "Modulus of Elasticity," accessed October 27, 2025, https://www.instron.com/en/resources/glossary/modulus-of-elasticity/.
51. Ghojel, J.I., "Review of the Development and Applications of the Wiebe Function: A Tribute to the Contribution of Ivan Wiebe to Engine Research," *International Journal of Engine Research* 11, no. 4 (2010): 297-312, doi:https://doi.org/10.1243/14680874JER06510.
52. Worm, J., Michalek, D., Naber, J., and Cooney, C., "Wiebe Function Parameter Determination for Mass Fraction Burn Calculation in an ETHANOL-GASOLINE Fuelled SI Engine," *Journal of Kones* 15, no. 3 (2008): 567-574.
53. Nagase Chemtex Co., Ltd., "Elongation Ranking of Resins & Rubbers," accessed October 28, 2025, https://group.nagase.com/nagasechemtex/e1/en/advanced-concept-materials/rubber-like-resin/resins-rubbers-elongation-ranking/.
54. Grasland, F., Chazeau, L., Chenal, J.M., Caillard, J. et al., "About the Elongation at Break of Unfilled Natural Rubber Elastomers," *Polymer* 169 (2019): 195-206, doi:https://doi.org/10.1016/J.POLYMER.2019.02.032.
55. Li, T., Wang, B., and Zheng, B., "A Comparison between Miller and Five-Stroke Cycles for Enabling Deeply Downsized, Highly Boosted, Spark-Ignition Engines with Ultra Expansion," *Energy Conversion and Management* 123 (2016): 140-152, doi:https://doi.org/10.1016/j.enconman.2016.06.038.
56. Lacerda, A., de Souza, G.R., Brito, J.N., Soto, F. et al., "Numerical Study to Achieve Low Fuel Consumption and Nitrogen Oxides Emissions in a Split-Cycle Engine Adapted from the Conventional Architecture," *SAE Int. J. Engines* 14, no. 2 (2021): 263-275, doi:https://doi.org/10.4271/03-14-02-0016.
57. Morgan, R., Lenartowicz, C., Vogiatzaki, K., Harvey, S. et al., "The Ultra Low Emissions Potential of the Recuperated Split Cycle Combustion System," SAE Technical Paper 2019-24-0189 (2019), doi:https://doi.org/10.4271/2019-24-0189.
58. Ortolani, P., Evans, K., and Treccarichi, F., "Cylinder Head Insulation Plate, Design, Analysis and Testing for an Extreme High Efficiency Internal Combustion Engine," SAE Technical Paper 2024-01-2831 (2024), doi:https://doi.org/10.4271/2024-01-2831.
59. Noga, M., "Five-Stroke Internal Combustion Engine—Yesterday, Today and Tomorrow," *IOP Conference Series: Materials Science and Engineering* 421, no. 4 (2018): 042058, doi:https://doi.org/10.1088/1757-899X/421/4/042058.
60. Noga, M. and Sendyka, B., "Determination of the Theorethical and Total Efficiency of the Five-Stroke SI Engine," *International Journal of Automotive Technology* 15, no. 7 (2014): 1083-1089, doi:https://doi.org/10.1007/s12239-014-0112-9.
61. Melin, A., Kittelson, D., and Northrop, W.F., "Parametric 1-D Modeling Study of a 5-Stroke Spark-Ignition Engine Concept for Increasing Engine Thermal Efficiency," SAE Technical Paper 2015-01-1752 (2015), doi:https://doi.org/10.4271/2015-01-1752.
62. Ailloud, C., Delaporte, B., Schmitz, G., Keromnes, A. et al., "Development and Validation of a Five Stroke Engine," SAE Technical Paper 2013-24-0095 (2013), doi:https://doi.org/10.4271/2013-24-0095.
63. Machado, T. and Monhol, F., "Comparative Thermal Efficiency Analysis between a 4-Stroke Engine versus a 6-Stroke Steam Injection Engine," SAE Technical Paper 2020-36-0217 (2021), doi:https://doi.org/10.4271/2020-36-0217.

Supplementary Materials

TABLE S.1 Measurement instruments and sensors used in the experiment, including range and specifications.

AVL GH 13Z-24 piezoelectric pressure transducer	
Sensitivity 0–150 bar	15.95 pC/bar
Measuring range	250 bar
Temperature range	400°C
Sensitivity at 250°C	15.82 pC/bar
AVL IndiModul 621 multi-channel data acquisition system	
Number of measurement channels	8
Analog inputs	± 10 V
ADC data recording rate	14-bit/800 kHz
Digital input (2 channels)	8-bit TTL-compatible
Crank angle mark and trigger signal input	2 inputs (TTL level)
AVL Flexifem Piezo amplifier 2P2E	
Output signal	–11V ... 11V (± 30 mA)
Linearity error	<0.01% FSO
Gain error	8 pC/V ... 25 pC/V ±0.5%
Gain resolution	12-bit
HBM force transducer S2	
Measuring element	Strain gauges
Rated force	500 N
Accuracy class	0.05
Rated sensitivity	2 mV/V
Input resistance	>345 Ω
Output resistance	300–500 Ω
Relative sensitivity error	<±0.25%
Rel. tensile/compression sensitivity variation	<±0.1%
Rel. reversibility error (0.2 F_{nom} to $Fnom_)$	<0.1%
Linearity error	<0.05%
Electrical connections	Six-wire configuration
HBM RM4220 SG-transducer amplifier	
Accuracy class	0.1
Amplifier gain	Min 80; max 8500
Zero adjustment	±2.00 mV/V
Bridge excitation voltage	5/10 V DC
Output voltage	0 ... 10 or ±10 V
Max non-linearity FSO %	G = 1000 (±0.001)
Nissan 22100-71J00 Crank Angle Sensor	
Number of reference marks	360
Crank angle sensor type	Photodiode optical encoder (360-slot disk)
Trigger sensor type	Photodiode optical encoder (1-slot disk)

FIGURE S.1 Motored torque of the membrane engine (black) and piston engine (blue) measured directly from the transducer with standard deviation error bars.

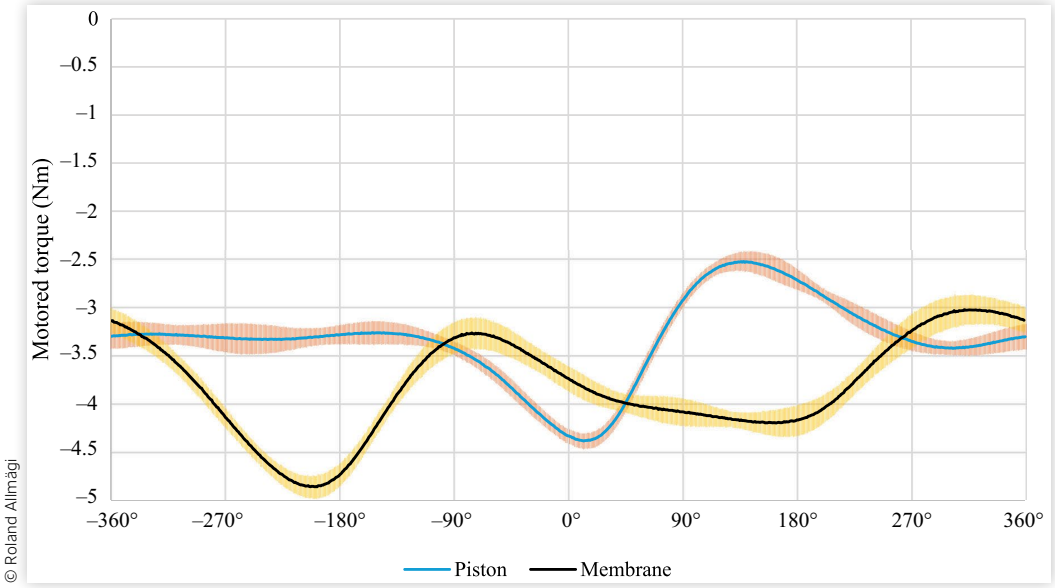

FIGURE S.2 Fired torque of the membrane engine (black) and piston engine (blue) measured directly from the transducer with standard deviation error bars.

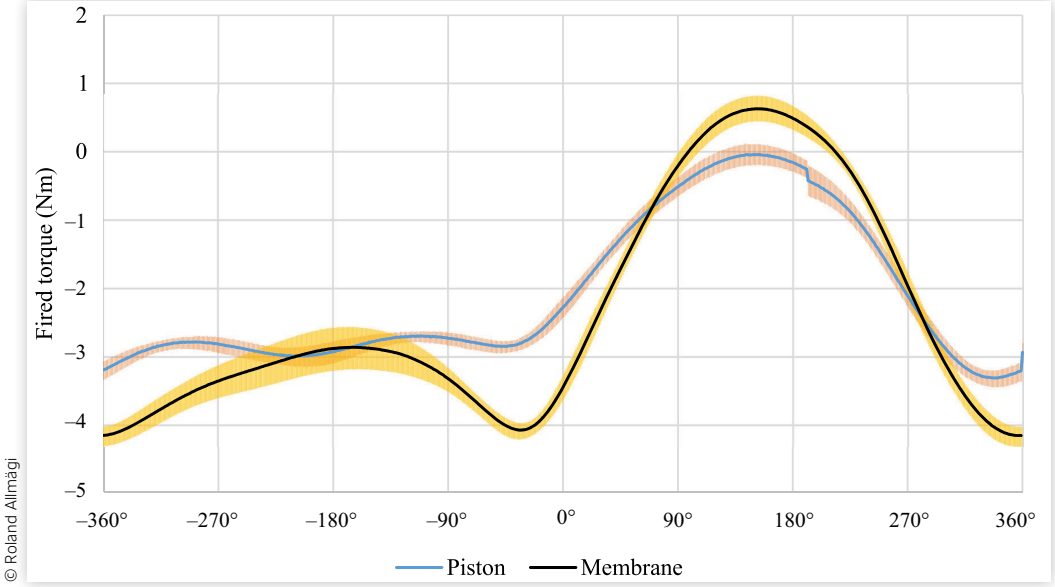

FIGURE S.3 Indicated cylinder pressure of the piston engine with standard deviation bars.

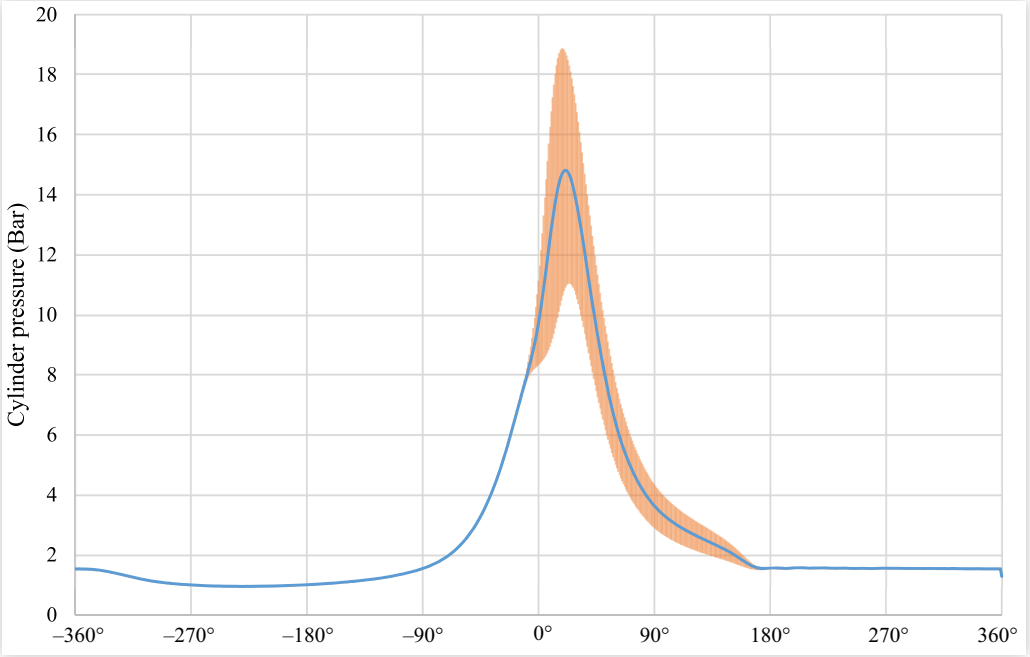

FIGURE S.4 Indicated cylinder pressure of the membrane engine with standard deviation bars.